# Zinc mobility and speciation in soil covered by contaminated dredged sediment using micrometer-scale and bulk-averaging X-ray fluorescence, absorption and diffraction techniques

M.-P. Isaure, Alain Manceau, Nicolas Geoffroy, Agnès Laboudigue, Nobumichi Tamura, Matthew A Marcus

# Zinc mobility and speciation in soil covered by contaminated dredged sediment using micrometer-scale and bulk-averaging X-ray fluorescence, absorption and diffraction techniques

Marie-Pierre Isaure[1,2], Alain Manceau[1*], Nicolas Geoffroy [1], Agnès Laboudigue[2], Nobumichi Tamura[3], Matthew A. Marcus[3]

[1] Environmental Geochemistry Group, LGIT- Maison des Géosciences, University J. Fourier and CNRS, 38041 Grenoble cedex 9, France

[2] Centre National de Recherche sur les Sites et Sols Pollués, 930 Boulevard Lahure, BP537, 59505 Douai cedex, France

[3] Advanced Light Source, Lawrence Berkeley National Laboratory, One Cyclotron Road, Berkeley, California 94720, USA

* Corresponding author: Alain.Manceau@ujf-grenoble.fr
Keywords: SXRF, EXAFS, XRD, speciation, Zn, sediment, soil
Running Title: Zn speciation in soil contaminated by dredged sediment

**ABSTRACT**

The mobility and solid-state speciation of zinc in a pseudogley soil (pH = 8.2-8.3) before and after contamination by land-disposition of a dredged sediment ([Zn] = 6600 mg $kg^{-1}$) affected by smelter operations were studied in a 50 $m^2$ pilot-scale test site and the laboratory using state-of-the-art synchrotron-based techniques. Sediment disposition on land caused the migration of micrometer-sized, smelter-related, sphalerite (ZnS) and franklinite ($ZnFe_2O_4$) grains and dissolved Zn from the sediment downwards to a soil depth of 20 cm over a period of 18 months. Gravitational movement of fine-grained metal contaminants probably occurred continuously, while peaks of Zn leaching were observed in the summer when the oxidative dissolution of ZnS was favored by non-flooding conditions. The Zn concentration in the <50μm soil fraction increased from ~61 ppm to ~94 ppm in the first 12 months at 0-10 cm depth, and to ~269 ppm in the first 15 months following the sediment deposition. Higher Zn concentrations and enrichments were observed in the fine (<2 μm) and very fine (<0.2 μm) fractions after 15 months (480 mg $kg^{-1}$ and 1000 mg $kg^{-1}$, respectively), compared to 200 mg $kg^{-1}$ in the <2 μm fraction of the initial soil. In total, 1.2 % of the Zn initially present in the sediment was released to the environment after 15 months, representing an integrated quantity of ~4 kg Zn over an area of 50 $m^2$. Microfocused X-ray fluorescence (XRF), diffraction (XRD) and extended X-ray absorption fine structure (EXAFS) spectroscopy techniques were used to image chemical associations of Zn with Fe and Mn, and to identify mineral and Zn species in selected points-of-interest in the uncontaminated and contaminated soil. Bulk average powder EXAFS spectroscopy was used to quantify the proportion of each Zn species in the soil. In the uncontaminated soil, Zn is largely speciated as Zn-containing phyllosilicate, and to a minor extent as zincochromite ($ZnCr_2O_4$), $^{IV}$Zn-sorbed turbostratic birnessite (δ-$MnO_2$), and Zn-substituted goethite. In the upper 0-10 cm of the contaminated soil, about 60 ± 10 % of total Zn is present as ZnS inherited from the overlying sediment. Poorly-crystalline Zn-sorbed Fe (oxyhydr)oxides and zinciferous phyllosilicate amount to about 20-30 ± 10 % each and, therefore, make up most of the remaining Zn. Smaller amounts of franklinite ($ZnFe_2O_4$), Zn-birnessite and Zn-goethite were also detected. Further solubilization of the Zn inventory in the sediment, and also remobilization of Zn from the poorly-crystalline neoformed Fe (oxyhydr)oxide precipitates, are expected over time. This study shows that land deposition of contaminated dredged sediments is a source of Zn for the covered soil and, consequently, presents environmental hazards. Remediation technologies should be devised to either sequester Zn into sparingly soluble crystalline phases, or remove Zn by collecting leachates beneath the sediment.

## 1. INTRODUCTION

Dredging operations carried out on waterways generate high volumes of sediments, which are generally deposited on soils along banks or in landfills. For example, several millions of tons of dredged sediment are generated every year in northern France and, until recently, were systematically spread over nearby soils. In industrialized areas, these sediments are often contaminated with heavy metals and this practice endangers the local environment and affects the safety of food and drinking water. The concentration and leaching behavior of metals in surface soils from abandoned dredged sediment disposal sites have been investigated previously, but not the form of metals (Tack et al., 1999; Vandecasteele et al., 2002). Since the mobility of metal contaminants depends on the nature of their interactions with solid constituents, knowing the amount and solid-state form of secondary anthropogenic metal species formed after the release of metals from deposited sediments is important for risk assessment.

Although there may be a multitude of metal uptake mechanisms in multi-elemental and multi-phase environmental materials, recent studies by extended x-ray absorption fine structure (EXAFS) spectroscopy have shown that metals generally exist in a restricted number of dominant secondary forms in a given matrix (Manceau et al., 2002a). Many uptake mechanisms, which had been described in the laboratory over the past decades, have now been identified in nature, including complexation with soil organic matter, adsorption on mineral surfaces, incorporation in mineral structures through coprecipitation or lattice diffusion, and metal precipitation (Cotter-Howells et al., 1994; Manceau et al., 1996, 2000a, 2002b, 2003, 2004; Hesterberg et al., 1997; O'Day et al., 1998, 2000; Hochella et al., 1999; Morin et al., 1999; 2001; Ostengren et al., 1999; Hansel et al., 2001; Caroll et al., 2002; Isaure et al., 2002; Kneebone et al., 2002; Roberts et al., 2002; Scheinost et al., 2002; Strawn et al., 2002; Jeong and Lee, 2003; Juillot et al., 2003; Kirpichtchikova et al., 2003; Paktunc et al., 2004; Sarret et al., 2004). While EXAFS spectroscopy has provided one of the cornerstones of heavy metal speciation science, most studies have been restricted to average structural properties because of the millimeter to centimeter dimension of the X-ray beam. Powder EXAFS performed on a bulk sample is needed to determine percentages of the representative metal species, but this method has low sensitivity to individual species in multi-component matrices. This technique can be complemented by other approaches in which individual species are unambiguously identified prior to their quantification by bulk averaging EXAFS spectroscopy. Attempts to reduce the number of species in natural samples prior to bulk EXAFS spectroscopic analysis have been made. These include fractionating the soil physically by density or size separation in solution or chemically with extractants (e.g., Isaure et al., 2002; Scheinost et al., 2002; Kim et al., 2003; Juillot et al., 2003). As practical and common as these methods are, none is fully satisfying because the very chemistry one is trying to probe may be modified, regardless of whether they are applied separately or collectively. Several limitations have been recognized: one is that extractants cannot discriminate single metal species nor discrete geochemical phases, and another is that trace metals become readsorbed and redistributed when soils are placed in solutions (Ostergren et al., 1999).

The alternative to physical and chemical separation is to probe the metal species individually in an undisturbed sample using a micrometer-sized X-ray beam (Manceau et al.,

2000a, 2002a,b; Roberts et al., 2002; Strawn et al., 2002). The task is relatively easy for primary minerals because the metal is locally concentrated in 'hot-spots' and incorporated in a crystalline solid, yielding an intense EXAFS signal. More difficult is the identification of secondary species because fine-grained minerals are often mixed at the micrometer scale and the metal may be bound at the mineral surface, yielding a weaker signal. Additional tools are then needed to ascertain the nature of the host mineral, or at least reduce the number of mineral candidates. This information can be obtained using X-ray microfluorescence (μ-SXRF) and microdiffraction (μ-XRD) as an adjunct to μ-EXAFS (Manceau et al., 2002a,b). μ-SXRF is applied to map elemental content and distribution, and is followed by μ-XRD from selected points-of-interest (POIs) to identify the nature of the crystalline phase(s) in the probed sample volume. Then, μ-EXAFS identifies the molecular-mechanism of the metal binding by the host phase(s), and may also help differentiate two host candidates as long as they have a contrasted local structure or chemical composition.

In the present work, all these bulk averaging and micrometer resolved X-ray techniques were combined to study Zn speciation in a soil affected by a disposed dredged sediment. The complexity of trace metal associations in contaminated soil increases because signal comes from both the polluting species and the geochemical background and, consequently, this new case study provides an opportunity to evaluate the capabilities of this new combined analytical approach to distinguish the two types of metal species.

## 2. MATERIALS AND METHODS

### 2.1 Experimental pilot site

A pilot site was set up in July 1997 near the town of Douai in northern France. An area of agricultural land 50 $m^2$ wide x 0.40 m deep was excavated, and the resulting basin was covered with a 0.40 m-thick layer of sediment dredged from the Scarpe canal as in a landfill. This canal has been used for almost one century to ship sulfide ores to a local Zn smelter, and has led to the contamination of the sediment ([Zn] = 6600 mg $kg^{-1}$). The groundwater table at the experimental plot is at a depth between 0 m in the flooded periods and 1.10 m in the non-flooded periods. Soil water was collected at depths of 40 cm (i.e., at the sediment-soil interface) and 70 cm in porous teflon cups.

### 2.2 The uncontaminated soil

The 0-20 cm soil layer below the sediment (i.e., 40-60 cm depth before excavation) was sampled for chemical, mineralogical and Zn speciation analyses before its covering with the sediment. The soil is similar to pseudogley leached soils (Luvisol Redoxisol) from the northern region of France. It is calcareous and silty, and contains millimeter-sized black and reddish nodules. Deeper layers have an increasingly clayey texture. The <50 μm fraction of the studied soil layer amounts to 82 wt. %, and the <2 μm clay fraction 12 wt. %, of the total soil. Coarse particles (> 500 μm) account for less than 1% in weight and are mainly composed of carbonaceous shell fragments. The bulk soil consists predominantly of quartz, calcite, feldspars and clay minerals as determined by XRD analysis (Table 1). The oriented <2 μm clay fraction

consists of kaolinite, illite, smectite and chlorite. The studied horizon is alkaline (pH = 8.2-8.3) and contains relatively little organic carbon (1%, measured by subtracting the inorganic carbon content from the total carbon content). The cation composition of carefully homogenized size fractions was analyzed in triplicate by inductively coupled plasma atomic emission spectrometry (ICP-AES) after digesting 0.5 g in teflon bombs with a mixture of concentrated HF (9 mL) and $HNO_3$ (1 mL). The bombs were placed in a microwave oven and heated to 200°C for 1h. After evaporation of the solution, the residue was redissolved into 3 mL of 6 N HCl and analyzed in triplicate. Zn concentration equals 45 mg $kg^{-1}$ and is comparable to the regional geochemical background (20-50 mg $kg^{-1}$, Baize 1997). The Zn content in the <50 µm fraction is 61 mg $kg^{-1}$, which means that Zn is almost uniquely present in the fine fraction since 61 mg $kg^{-1}$ x 0.82 = 50 ~ 45 mg $kg^{-1}$. The Zn concentration in the clay fraction (<2 µm) (200 mg $kg^{-1}$) is 4.4 times higher than in the bulk sample, and since this fraction amounts to 12 wt. %, it contains ~53 % of the total soil Zn. Unperturbed soil samples were sampled at 0-10 and 10-20 cm depths for speciation analysis. These samples were dried overnight in an oven, impregnated with Scotchcast™ epoxy (3M company), a high purity resin, and prepared as thin sections mounted on quartz slides.

### 2.3 The contaminated dredged sediment

Zn speciation in the sediment was studied previously (Isaure et al., 2002). The metal is preferentially concentrated in the 500-2000 µm, 2-20 µm and <2 µm fractions, with the coarse fraction being enriched in primary and the fine fraction into secondary Zn species. In the freshly dredged, unaerated, sediment, Zn is overwhelmingly speciated as sphalerite (ZnS), and to a lesser extent as zincite (ZnO) and willemite ($Zn_2SiO_4$). In contact with atmosphere, oxidation of ZnS releases Zn into solution which is partly retained within the sediment by ferric (oxyhydr)oxides and phyllosilicates, the remainder being leached to the underlying substrates.

### 2.4 Water and contaminated soil sampling

Water accumulated in porous cups was collected twice a week during the first 15 days following the installation, once a week during the following month and a half, and finally once every two weeks from September 1997 to December 1999. Solutions were sampled using a vacuum pump. Eh and pH were measured in the field in extracted solutions sampled at 40 cm depth, and acidified with $HNO_3$ and filtered with a 0.45µm filter before analysis by ICP-AES. Soil samples were collected with a drill at 0-10 cm and 10-20 cm below the sediment-soil interface (i.e. 40-50 cm and 50-60 cm below the surface) every two to six months over a period of 18 months following the sediment deposition. The upper (0-10 cm) and lower (10-20 cm) samples were air-dried, homogenized, and wet-sieved at 50 µm in deionized water. Since more than 80 % of the soil particles are contained in the <50 µm fraction, this size fraction was considered representative of the bulk soil. The <0.2 µm fraction was extracted by continuously centrifuging the <2 µm fraction at 5000 rpm with a 150 $mL.min^{-1}$ flow. These soil samples were chemically analyzed as described in section 2.2 and some of them were used for Zn speciation analysis. Unperturbed soil was sampled at 0-10 and 10-20 cm depths after 27 months of sediment deposition, and thin sections were prepared as described in 2.2.

## 2.5 Zn speciation analysis

**2.5.1 Synchrotron-based micro X-ray fluorescence (µ-SXRF).** X-ray fluorescence spectra were recorded on Beamline 10.3.2 at the Advanced Light Source (ALS), Berkeley (Marcus et al., 2004). Fe, Mn and Zn µ-SXRF elemental maps were obtained by scanning the soil thin-sections under a monochromatic beam with an energy of 10 keV and a beam size on the sample of 16 µm (H) x 5 µm (V) full width at half maximum (FWHM), while recording the X-ray fluorescence with a 7-element Ge solid-state detector. The step size was 20 x 20 µm and the dwell time 400 ms/point.

**2.5.2 EXAFS spectroscopy.** Zn and Mn K-edge µ-EXAFS spectra were collected on the same beamline as µ-SXRF on points-of-interest (POIs) selected from the elemental maps. Measurements were performed in fluorescence-yield detection mode using the same 7-Ge detector as for µ-SXRF measurements and at 16 µm x 5 µm lateral resolution. Zn K-edge P-EXAFS and powder EXAFS experiments were performed on beamline FAME (BM32b) at the European Synchrotron Radiation Facility (ESRF, Grenoble, France). Spectra were collected in fluorescence detection mode using a 30-element Ge solid-state detector. P-EXAFS measurements were carried out on self-supporting films (SSF) prepared from the <0.2 µm fraction at incident angles between the electric field vector and the film plane of $\alpha$ = 10°, 35° and 80° (Manceau et al., 1998). Powder EXAFS measurements were performed on pressed pellets from the <50 µm soil fraction at the magic angle ($\alpha$ = 35°, Manceau et al., 1988).

EXAFS $\chi(k)$ functions were derived from X-ray absorption spectra by modeling the post-edge atomic absorption with a spline function and normalizing the signal amplitude to unit step in the absorption coefficient. The $E_0$ value was taken to be the half-edge-jump point. The rationale for this choice was discussed by Manceau et. al. (1996, 2002a). Radial structure functions (RSFs) were obtained by Fourier transforming $k^3$-weighted $\chi(k)$ spectra using a Kaiser window. The abscissae of RSF plots ($R+\Delta R$) correspond to interatomic distances uncorrected for phase shift (Teo, 1986). EXAFS spectra also were least-squares fitted to a combination of reference spectra. The library of EXAFS standards (Manceau et al., 2003) includes a large number of primary and secondary Zn minerals and precipitates, mineral surface sorption complexes at various loadings, and Zn-organic complexes. The fractional contribution of each model spectrum to the best fit is directly proportional to the amount of Zn present in that form in the sample (Manceau et al., 1996). The residual *Res* parameter, defined as $Res = \Sigma( k^3\chi_{exp} - k^3\chi_{model})^2 / \Sigma (k^3\chi_{exp})^2$, was used as the fit criterion, a lower *Res* value representing a better match between experimental and reference spectra. The precision on the proportion of species in a mixture was estimated to be 10 % of total Zn by varying the fractional amount of each component until *Res* increased by at least 15 %. The addition of a new component in the fit was considered meaningful if *Res* decreased by at least 20 %.

**2.5.3 Micro X-ray diffraction (µ-XRD).** µ-XRD patterns were recorded on beamline 7.3.3 at the ALS using a 1024 x 1024 pixels Bruker CCD camera and an exposure time of 10 min. They were collected at selected points-of-interest (POIs) in reflection geometry mode by

inclining the sample thin-sections at 6°θ (Manceau et al., 2002a). At this angle, the lateral beam size on the sample is 14 µm (H) x 11 µm (V). To suppress the background noise arising from the Mn, Fe, and Zn Kα fluorescence signals, the incident energy was set at 6.3 keV, i.e., below the Mn K-edge. In going from the 10.3.2 to the 7.3.3 beamline, the POIs were re-imaged by µ–SXRF.

## 3. RESULTS AND INTERPRETATIONS

### 3.1 Time fluctuations of pH, Eh, Zn, and Fe in the soil solution

The experimental plot was flooded in winter and drained in the summer. The Eh values measured in percolating water just below the dredged sediment layer varied from about 120 to 370 mV during the non-flooded period, and decreased to 50-100 mV during the winter (Fig. 1a). No measurements were performed during the summers of 1998 and 1999 due to the complete drying of the basin. The pH values varied between 6.8 and 8.1 when the basin was submerged and decreased to 6.1-6.3 during the non-flooding periods. The decrease in pH can be explained by the acidification of soil solutions resulting from the oxidative dissolution of metal sulfides ($FeS_2$ and ZnS) under oxic conditions during the summers. Similar seasonal variations in Eh and pH during drying and hydromorphic events were reported in a wetland (Bostick et al., 2001). Seasonal fluctuations were also observed for Zn and Fe concentration in the soil solution (Fig. 1b). Maxima in dissolved Zn and Fe concentrations were measured during the summery oxidative seasons with values peaking at 1.32 and 1.13 mg $l^{-1}$, respectively, in the late spring of 1998, and at 3.85 and 1.34 mg $l^{-1}$ in the late spring of 1999. During the flooded periods, less Fe and Zn were leached out despite the low Eh value which is expected to favor the release of $Fe^{2+}$ ions to the water, as observed for example in paddy soils during submerged periods (Takahashi et al., 2004). The contrasting geochemical behavior of Fe in the sediment and paddy field results from a difference of mineral form, with solid Fe being reduced ($FeS_2$) in the sediment and oxidized (FeOOH) in the paddy field. The Fe release is controlled in one case by the reduction of Fe (oxyhydr)oxides, which occurs during flooding periods, and in the other by the oxidation of iron sulfides, which occurs during non-flooding periods. The parallel releases into solution of Fe and Zn indicates that dissolved Zn originates mainly from the oxidation of ZnS.

### 3.2 Evolution of Zn concentration in soil over time

The Zn concentration in the <50µm fraction increased from 61 to 94 mg $kg^{-1}$ in the 0-10 cm layer below the sediment-soil interface 12 months after deposition, and to 269 mg $kg^{-1}$ and 227 mg $kg^{-1}$ after 15 and 18 months, respectively (Fig. 2). The difference in concentration between the 15 and 18 months measurements is probably insignificant and likely stems from lateral compositional heterogeneity. A similar apparent decrease in Zn concentration was observed after 9 months. Zn also increased over time in the 10-20 cm layer, but more moderately as expected for a plume of contamination emanating from the overlying sediment. Zn content was also measured in the fine fractions. After 15 months, Zn concentration was 480 mg $kg^{-1}$ in the <2 µm and 1000 mg $kg^{-1}$ in the <0.2µm fractions at 0-10 cm depth, compared to

200 mg $kg^{-1}$ in the <2 μm fraction of the initial soil. The higher Zn content of the smallest fraction is consistent with the higher surface reactivity of nanometer-sized particles and also with the possible vertical migration and precipitation of Zn-containing colloids. Results presented below show that the Zn in this size fraction is mostly sorbed on neoformed Fe (oxyhydr)oxides.

### 3.3 Speciation of Zn in the uncontaminated soil

**3.3.1 Elemental distribution by μ-SXRF**. Examination of the soil thin sections under a binocular lens showed the presence of millimeter-sized reddish concretions embedded in a fine clayey matrix. No Zn-rich regions or grains could be detected by coupled scanning electron microscopy – energy dispersive spectroscopy (SEM-EDS), even in the Fe aggregates, and synchrotron radiation had to be employed to visualize the trace metal distribution. Several sample regions were examined by μ-SXRF, and the mineralogy and crystal chemistry of Zn is completely represented by the two regions presented in Figures 3 (0-10 cm depth) and 4 (10-20 cm depth). Chemical maps recorded at 20 x 20 μm resolution showed that the soil is fine-grained and that the Fe concretions (colored in green on the maps) are aggregates of these fine-grained particles (Fig. 3a, 4a). The two Fe concretions mapped also contain higher amounts of manganese (colored in blue) than the matrix. Fe-Mn association is commonly observed in soils (Singh and Gilkes, 1996) because these two elements are both mobile in reduced form and immobile in oxidized form (Takahashi et al., 2004). Therefore, fluctuations of the redox potential induced by seasonal variation of the water table leads to the type of Fe-Mn concretionary features shown. While Mn was almost always associated only with Fe in the soil concretions, iron was also detected in the fine clayey matrix, probably in association with phyllosilicates and as finely dispersed Fe (oxyhydr)oxide coatings on primary and secondary mineral grains. When Zn is added in red to the two previous maps, 1-2 pixels wide, bright red hot-spots appear indicating that the highest Zn concentrations occur in Zn-rich micrometer-sized grains (Fig. 3b, 4b). A Zn-Mn association can be detected on the fringe of the ferromanganese concretion in Figure 4b as indicated by the violet color of the Mn area in RGB representation. The Mn oxide pocket in the interior of the Fe halo in Figure 3b seems to lack Zn because it is still colored blue in the tricolor map. However, this Mn pocket turned violet when the red (Zn) channel was made sensitive enough so that the pixel color saturated at a Zn level of 1/5 that of the maximum (Fig. 3c). This step was necessary because the hot-spots, which are more Zn-rich than the Mn pocket, set the scale for the red channel in Figure 3b. Therefore, the Mn pocket also contains Zn, but less than the other Fe-Mn concretion. This adjustment of the red channel also modified the color of the fine clay matrix at both 0-10 cm and 10-20 cm depth. It became reddish-brown, in contrast to the Fe halo, which remained bright green, indicating that the clay matrix contains Zn but not the Fe halo.

In total, three Zn populations with contrasting Zn concentrations could be highlighted by varying the saturation level for the red pixels as explained above: Zn-rich grains, Zn-Mn oxide, and Zn in the fine clayey matrix. Since Zn has an overall low concentration in the uncontaminated soil, these three populations were verified by mapping the same areas twice, once just above and once just below the Zn edge, then calculating the difference map between above- and below-edge signals. The difference maps have almost zero background count and,

consequently, Zn occurs at all grey pixels. These maps are imaged in inverse-contrast grayscale in Figures 3d and 4d. The Zn hot-spots now appear as black points disseminated in several parts of the pictures. The Zn-Mn association on the border of the Fe-Mn concretion found at 10-20 depth is confirmed, but this association is now clearly detected also in the center of the Fe halo from the upper soil wherever there is Mn. Adding the net Zn Kα intensity pixel by pixel would show that Zn is predominantly present in the fine matrix, especially in the upper soil. These pictures also show that the Fe areas in the Fe-Mn concretions are essentially Zn-free. This is particularly evident in Figure 3d since the trace of the Fe halo appears light gray in the Zn map. A few yellow spots (obtained by mixing red and green) in Figure 4c, which are dark gray on the grayscale map, suggest a fourth Zn species, probably a Zn-containing Fe (oxyhydr)oxide phase. This minor component was not analyzed by micro-EXAFS in the uncontaminated soil, but a similar spot was found in the contaminated soil and its analysis revealed Zn-containing goethite (see below).

**3.3.2 Mineralogical composition by μ-XRD**. Two-dimensional diffraction patterns were recorded at several POIs. No Zn-rich primary mineral could be detected at the Zn hot-spots, probably because these primary minerals often occur as micrometer-sized euhedral crystals (Nesterov and Rumyantseva, 1987) and, therefore, do not yield much, if any, diffracted beam in our experimental setup. In Mn-rich areas, broad diffraction maxima at 7.1-7.2, 2.4 and 1.42 Å match known diffraction peaks of turbostratic hexagonal birnessite (δ-$MnO_2$; Drits et al., 1997; Manceau et al., 2003, 2004) (Fig. 5a). This phase assignment was confirmed by observing the disappearance (1.42, 7.1-7.2 Å) or weakening (2.4 Å) of these broad peaks in a control XRD pattern a few tens of microns away from the probed Mn-rich spot (Fig. 5b). Other nano-divided mineral species identified by μ-XRD include dioctahedral smectite, generating continuous and homogeneous diffraction rings on the two-dimensional XRD patterns at 4.45-4.48 Å (020/110), 2.55-2.58 Å (130/200), and 1.50 Å (060), and poorly-crystalline iron (oxyhydr)oxides (FeOx) generating a broad reflection at ~1.6-1.7 Å. In addition to the large and continuous Debye rings from nanometer-sized particles, thin homogeneous to discontinuous spotty rings to even single spot reflections from fine crystallites and coarse grains were observed on the two-dimensional patterns. The identified minerals include quartz, calcite, dolomite, microcline, albite, analcime, anatase, ilmenite, mica, and goethite. The phyllosilicate rings were often spotty due to the mixing of large-grained micaceous particles to the fine-grained smectite. The μ-XRD patterns recorded in the Fe-rich areas typically differed from others by the enhancement of the broad bands at ~1.7 Å from FeOx material. Therefore, the Fe concretions are made of finely dispersed disordered ferric (oxyhydr)oxides. Crystalline, and often Zn-containing, goethite particles were detected as well. The pattern presented in Figure 5b shows the presence of large kaolinite crystals. This species was unambiguously identified by the spotty 001 reflection at 7.1-7.2 Å and the 060 reflection at 1.49 Å. Birnessite and kaolinite both yield a basal reflection at 7.1-7.2 Å, which generally hampers their distinction by conventional XRD. Differentiation is often possible by μ-XRD because the two minerals generally have a different grain size in soils and, consequently, a different two-dimensional distribution of X-ray intensity along the 001 ring

(Manceau et al., 2002b, 2004). Correlating μ-SXRF and μ-XRD data at the POI may help differentiate these two minerals since kaolinite does not contain manganese.

**3.3.3 Speciation of Zn by μ-EXAFS, P-EXAFS and powder EXAFS spectroscopy.** The form of Zn in the hot-spots and associated with Mn were identified by μ-EXAFS, and that of Zn in the fine clayey matrix by P-EXAFS. μ-EXAFS spectra were recorded at four different hot-spots and all showed that Zn occurred as one species, essentially identical to zincochromite ($ZnCr_2O_4$, Fig. 6a), previously identified in a pristine horizon of a clayey acidic soil (pH 4.5 – 5.0) from Ohio (Manceau et al., 2004). The systematic association of Zn and Cr in these grains was verified by point μ-SXRF analysis. To illustrate the spectral sensitivity of EXAFS to species determination, the hot-spot spectrum is compared in Figure 6b to that of zinc ferric spinel, franklinite ($ZnFe_2O_4$), in which chromium is replaced by iron. The two spectra have exactly the same shape, indicating that Zn occupies the same crystallographic site in the two structures, but a different phase with $ZnCr_2O_4$ being right-shifted to higher *k* values. This difference comes from the smaller size of $Cr^{3+}$ (0.61 Å) relative to $Fe^{3+}$ (0.64 Å), which results in a reduction of the Zn-Cr distances relative to Zn-Fe. The effect of the Fe for Cr substitution is more obvious in *R* space. Comparing the imaginary parts of Fourier transforms (Fig. 6c,d) for the unknown, $ZnCr_2O_4$, and $ZnFe_2O_4$, we find that there is a rightward shift of the features of the Zn-(Fe,Zn) peaks for $ZnFe_2O_4$ relative to $ZnCr_2O_4$, but no shift of the Zn-O peak. This observation can be explained by the fact that the Zn-O first shell distances are the same in the two spinels, but the Zn-Fe and Zn-Cr distances are not.

A good spectral match was obtained between the unknown and the Zn-sorbed birnessite reference μ-EXAFS spectra in the manganese-rich regions, as expected from μ-SXRF and μ-XRD results (POI-2 in Fig. 4, Fig. 7). We know from previous work (Lanson et al., 2002a; Manceau et al., 2002c) that Zn is sorbed in the interlayer of phyllomanganates on vacant layer Mn sites, and can be tetrahedrally or octahedrally coordinated depending on the detailed stoichiometry and stacking mode of the Mn layers. The μ-EXAFS spectrum and Fourier transform of the soil Zn-birnessite species are shown in Figure 7 along with those for Zn-sorbed birnessite references, in which Zn coordination is either fully tetrahedral ($^{IV}$ZnBi reference in Marcus et al., 2004) or 2/3 tetrahedral and 1/3 octahedral (ZnBi8 reference in Manceau et al., 2002c). A phase shift in both the *k* and *R* spaces are observed such that the sample has shorter bond distances than ZnBi8. In contrast, a perfect match is observed with the $^{IV}$ZnBi reference. The shorter Zn-O and Zn-Mn distances when Zn is only four-fold coordinated are understandable because Zn is smaller in tetrahedral (0.60 Å) than octahedral (0.74 Å) coordination. The Zn-Mn shell was fitted using FEFF-derived (Ankudinov et al., 1998) amplitude and phase shift functions for which $S_0^2$, $\sigma^2$, and $\Delta E_0$ were adjusted to match the second shell of chalcophanite ($^{VI}ZnMn_3O_7 \cdot 3H_2O$). The sample has a $^{IV}$Zn-Mn distance of 3.33 ± 0.02 Å, compared to 3.49-3.50 Å when Zn is octahedrally coordinated. In keeping with the results of Marcus et al. (2004) on marine Zn-containing birnessite, we found that this soil Zn-sorbed birnessite sample contains at most about 7 % $^{VI}$Zn.

In the two Zn species identified so far, Zn was associated with either Cr in zincochromite or Mn in birnessite, and the visualization of the Zn-Cr and Zn-Mn correlations by μ-SXRF helped identify these species. In contrast, in the clayey matrix Zn is associated with mineral

species containing low-Z elements (i.e., Mg, Al, Si), and μ-SXRF is uninformative about their possible nature. Using a low-energy excitation beam would not be conclusive either because Mg, Al and Si are background elements that are ubiquitous in the soil matrix. Since μ-XRD revealed the presence of smectites, and we know from previous work that Zn is frequently bound to hydrous silicates in soils (Manceau et al., 2000a, 2002a, 2003; Scheinost et al., 2002; Juillot et al., 2003), this candidate species was tested by P-EXAFS on the <0.2 μm fraction (sample Fine_Raw_SSF). Fig. 8a shows a strong angular dependence of the measured signal when the clay film is rotated relative to the electric field vector of the X-ray beam. The strength of the polarization dependence is high for the second oscillation with its maximum being shifted to higher *k* values upon increasing α angle, and the shoulder at 5.3 $Å^{-1}$ on its left tail being reinforced. A similar spectral evolution was observed for Zn sorbed on the edges of hectorite particles (Fig. 8b; Schlegel et al., 2001) and in substitution in montmorillonite from Redhill ([Zn] = 85 mg $kg^{-1}$, Redland Minerals), Survey, England (Fig. 8c). In these two references, Zn octahedra share edges with Mg/Al octahedra in the octahedral sheet and corners with Si tetrahedra in the tetrahedral sheet (Fig. 9). Detailed analysis of the P-EXAFS spectra for metal-sorbed and metal-containing phyllosilicates (Manceau et al., 1998, Schlegel et al., 1999, 2001) showed that the 5 $Å^{-1}$ region is sensitive to the metal-Si atomic pair, and that this contribution is reinforced when the out-of-plane structure of layer silicates is probed (α = 80-90°). Therefore, our experimental data provide strong evidence for the binding of Zn to phyllosilicate into the clayey soil matrix. Since kaolinite particles are coarse, they are absent or scarce in the <0.2 μm fraction. In addition, it is unlikely that their platelets were well oriented parallel to the film surface since individual kaolinite layers are not dispersed in solution, in contrast to smectite layers. Consequently, we conclude that the observed angular dependence stems from Zn-containing smectitic clays. Figures 10a and 10b show that the Zn-phyllosilicate species found in this study is similar as the one found in another soil from the same region studied previously (Manceau et al., 2000a), suggesting common structural principles in soils from this region of France. Therefore, the possible nature of the Zn-bearing clay and uptake mechanism of Zn are examined further below.

Three peaks, denoted B1, B2 and C, are observed in the Fourier transforms of the soil and Zn-sorbed hectorite EXAFS spectra (Fig. 10c,d). Schlegel et al. (2001) showed that in hectorite peak B1 originates from the first Mg (Oct1) and Si (Tet1) shells, peak B2 from the third oxygen shell (O3), and peak C from the second silicon shell (Tet2, Fig. 9b). In Zn-containing and Zn-sorbed Mg/Al phyllosilicates (i.e., hectorite, Mg-kerolite, montmorillonite), peak B1 always has a low intensity because of the destructive interference between the contributions from the Zn-Oct1 and Zn-Tet1 pairs. In contrast, this peak is intense when a metal is surrounded by high-Z atoms, such as in nontronite ($Fe^{3+}$) and pure Zn-kerolite (Zn). Therefore, its weakness in the soil sample is an indication of the association of Zn with 'light' atoms.

The possibility of the incorporation of Zn in the phyllosilicate structure was examined by comparing the unknown spectrum with a series of Zn-substituted phyllosilicate references. The best spectral matches were obtained with low-Zn kerolite (ZnKer070 $Si_4(Zn_{0.7}Mg_{2.3})O_{10}(OH)_2.nH_2O$) (Fig., 10e,f) and the Redhill and SAz-1 (Source Clay Minerals Repository of the Clay Minerals Society, [Zn] = 36 mg $kg^{-1}$) natural montmorillonites (Fig. 10g-j). In all these compounds, Zn octahedra are linked only or predominantly to light atoms,

as seen from the shape of the Fourier transforms (Fig. 10f,h,j), and this common structural characteristic with Zn-sorbed hectorite is another indication of the absence of Zn domains in the soil zinciferous phyllosilicate. However, the agreement between experiment and model was poorer with all Zn-substituted references than with Zn-sorbed hectorite and, consequently, the data are best described by the formation of a surface complex on the layer edge of a magnesium hydrous silicate. Since EXAFS cannot differentiate Mg from Al, the presence of some Al atoms in the coordination sphere of Zn is not excluded, but the amount of Al should be low enough for the local structure to remain trioctahedral.

With μ-EXAFS we look at an infinitesimally small portion of the bulk soil sample, and the representativity of metal species identified at the micrometer scale needs to be assessed by determining the proportion of each species in the soil volume. This was performed by recording the powder EXAFS spectrum of the <50 μm fraction, which represents more than 80% of the total soil. Figure 11 shows that the <50 μm and <0.2 μm fractions have essentially the same powder EXAFS spectra (i.e., similar Zn speciation). Spectral simulations showed that $ZnCr_2O_4$ and $^{IV}$ZnBi together amount to less than 10 % of the spectral signal. Thus, the results are consistent with Zn being largely bound to phyllosilicate with lesser amounts in zincochromite and Zn-sorbed birnessite.

### 3.4 Speciation of Zn in the contaminated soil

**3.4.1 Elemental distribution by μ-SXRF.** The Fe-Mn bicolor map from the contaminated soil thin section at 5-10 cm beneath the sediment shows the occurrence of a coarse, ~1500 μm in size, Zn-containing slag in the upper left side of the mapped area, and several dozen round- to oval-shaped Fe-rich and Mn-rich micrometer grains (Fig. 12a,b). Similar coarse anthropogenic products were observed in the dredged sediment (Isaure et al., 2002), and their presence in the underlying soil results from gravitational transfer. Four elemental associations were identified from the analysis of the four-fold red-saturated ($I_{Max}$ = $I(Zn\text{-}K\alpha)_{Max}/4$) Zn-Fe-Mn tricolor map and from the recording of X-ray fluorescence spectra at numerous POIs: Fe-containing Zn hot-spots, Zn-Mn association in Mn-rich grains, Zn-Fe association throughout the fine ferruginous soil matrix, and Zn-Fe-Ca association in the coarse slag and in smaller slag grains dispersed in the soil matrix. A selection of characteristic point X-ray fluorescence spectra is shown in Figure 13a-e. Zn hot-spots have a Fe(Kα):Zn(Kα) ratio close to 1, which suggests a primary Fe-Zn mineral (POI-1). The Mn grains at POIs 2 and 3 have Mn(Kα):Fe(Kα) and Mn(Kβ):Zn(Kα) ratios of 100:80:19 and 54:100:8, respectively. These ratio changed to 2:100:3 and 1:100:2 when the fluorescence spectra were taken in the fine matrix a few micrometers away from the center of the grains, which indicates a Mn-Zn association and is consistent with the violet color of the Mn grains in the tricolor map (Fig. 12b). By referring to results from the uncontaminated soil, it appears that Zn is likely speciated as $^{IV}$Zn-sorbed birnessite in the Mn-rich spots. The residual Zn-Kα intensity when the beam was not on the Mn grains stemmed from the background contribution of Zn in the ferruginous clayey matrix. The ratio of Fe(Kα) to Zn(Kα) was about halved from the upper to the lower region of the map as indicated by the change of the matrix cast from reddish-brown to green in the RGB picture. This gradient in color is consistent with a diffusion of contamination at 10 cm depth from the overlying

sediment. The fourth Zn pool is characterized by the systematic presence of Ca and Cu in addition to Fe and Zn (POIs 4 and 5). This compositional signature is characteristic of (Zn,Fe)S-rich slag and dust (Sobanska et al., 1999; Isaure et al., 2002), and was detected, not only on the rim of the coarse particles from the smelting process, but also in many spots within the fine matrix.

The green cast of the argillaceous matrix at 10-20 cm depth was not modified when the intensity of the red color, coded for Zn, was increased four times (Fig. 12c,d). Therefore, anthropogenic zinc did not penetrate the clayey matrix at this depth 27 months after deposition of the sediment. However, the soil matrix is speckled with ten to forty micrometer-sized Zn-rich grains, which are partly anthropogenic according to point μXRF analysis. Three types of exogenous grains could be defined on the basis of their elemental composition: Zn-rich, Ca- and Cu-free, primary grains having a Zn(Kα):Fe(Kα) ratio equal or higher than 1 (e.g., POI-6), Ca- and Cu-containing Zn-rich grains having a variable Zn(Kα):Fe(Kα) ratio, that is a variable ZnS/FeS ratio (e.g., POI-7), and Zn-depleted ferruginous grains having a Fe(Kα): Zn(Kα) ratio equal to about 6-7 (POI-8, Fig. 13f-h). Only one specimen of this last grain, colored in orange in the tricolor map, was found.

**3.4.2 Mineralogical composition by μ-XRD**. The μ-XRD pattern from the clayey matrix has dominant reflections from quartz and dioctahedral phyllosilicate (9.9–10, 4.45-4.48, 2.55-2.58, 1.50 Å), and minor reflections from kaolinite, calcite, albite, ilmenite, anatase, mullite ($Al_4Si_2O_{10}$), and from poorly-crystalline Fe (oxyhydr)oxides (FeOx) as indicated by the broad scattering bands at 1.98-2.0, 1.6-1.7, and 1.5 Å (Fig. 14a). The 1.98-2.0 Å band is generally used to differentiate six-line ferrihydrite from feroxyhite, but phase identification is equivocal because phyllosilicates have a reflection at about the same position. Mullite undoubtedly has an anthropogenic origin. It is a high-temperature mineral, which is present in the sediment (Isaure et al., 2002), and was identified in a nearby Zn smelter waste (Thiry et al., 2002). The diffractogram taken at the Mn-Zn rich spot (POI-2 in Fig. 12b) is essentially the same as the pattern from the matrix (Fig. 14b). The differences between the two XRD traces, which provide the most insight, are the broadening of the 7.1-7.2 Å basal reflection, the reinforcement of the peak at 2.4-2.5 Å relative to the 2.5-2.6 Å peak, and the presence of a new peak at 1.42 Å, at POI-2. These scattering features are indicative of turbostratic birnessite.

**3.4.3. Speciation of Zn and Mn by μ-EXAFS, P-EXAFS and powder EXAFS spectroscopy**. No μ-EXAFS spectrum was recorded from the Ca- and Cu-containing slag material because Zn is mainly present as ZnS in this refractory product of the smelting process (Isaure et al., 2002), and the occurrence of this species in the top soil will be established below by powder EXAFS. Several Zn K-edge μ-EXAFS spectra from individual micrometer-sized Zn-rich grains dispersed in the fine matrix were collected. Franklinite was identified at POI-1 in Figure 12b. The Zn-rich grains observed at 10-20 cm depth either had a pure $ZnFe_2O_4$ or a mixed $ZnFe_2O_4$-$ZnAl_2O_4$ composition, suggesting the presence of a gahnite-franklinite phase mixture or solid solution $(Zn(Fe,Al)_2O_4$, Figure 15a). The Zn K-edge μ-EXAFS spectrum taken at POI-8 was well reconstructed with a mixture of 61 % Zn-substituted goethite and 37 % franklinite, suggesting that franklinite started to weather and that the weathered Zn was

incorporated into a neoformed goethite precipitate at the surface of the Zn-Fe spinel (Fig. 15b). The Zn μ-EXAFS spectrum collected at POI-2 has some obvious similarities but is not identical to that collected in the Mn-rich region of the non-contaminated soil (Fig. 15c). The two spectra essentially differ by the split of the second oscillation, which is deep when all the Zn sits on top of vacancy sites in manganese layers (Fig. 7e,f), but less pronounced when Zn is present in several structural environments (Manceau et al., 2002c). Fourier transformation to the *R* space shows that the Zn-Mn pair at $R + \Delta R \sim 3$ Å, characteristic of the corner-sharing interlayer $^{IV}$Zn – layer Mn interaction in pure Zn phyllomanganates, is still present in the unknown but its amplitude is lowered and its maximum slightly rightward shifted (Fig. 15d). The most likely explanation is that there is a mixture of Zn-birnessite with other Zn species, such as Zn-bound Fe (oxyhydr)oxides and phyllosilicates, which are abundant in the upper matrix of the contaminated soil (see below), but also Zn-bound phosphates whose spectra have some overall similarities with the unknown spectrum. Since the speciation of Zn differs from the one commonly found at Mn-rich spots (Manceau et al., 2000a, 2003; Marcus et al., 2004), the Mn K-edge EXAFS spectrum was recorded to gain further insight into the structural chemistry of this soil birnessite.

Recent studies of a large series of birnessite species showed that Mn-EXAFS spectra are sensitive to the $Mn^{3+}/Mn^{4+}$ ratio in the sample, the amount and ordering of $Mn^{3+}$ in the manganese layer, and the amount of corner-sharing interlayer cation polyhedra above layer vacancy sites (Manceau et al., 1997, 2004; Gaillot et al., 2003; Marcus et al., 2004). The frequency of the 'staircase' region around 4-6 $Å^{-1}$ was shown to vary with the amount of $Mn^{3+}$ in the sample. A shift to the left of the electronic wave is observed in this region when the trivalent manganese content is high, as in lithiophorite ($Mn^{3+}/Mn^{4+}$ = 0.47; Yang and Wang, 2003) and in triclinic birnessite (TcBi, $Na_{0.31}(Mn^{4+}_{0.69}Mn^{3+}_{0.31})O_2 \cdot 0.40H_2O$; Silvester et al., 1997) (Fig. 16a,b). This shift can be explained with reference to the fact that the $Mn^{3+}$ ion is bigger than the $Mn^{4+}$ ion, thus the Mn-O and Mn-Mn distances will depend on the overall trivalent manganese fraction. Comparison of the unknown sample with a large series of birnessite references having different, but well-known, $Mn^{3+}/Mn^{4+}$ ratios led us to conclude that the soil birnessite has little (<10 %) $Mn^{3+}$. The second indicator region is the shape of the left tail of the second EXAFS oscillation at 6-7 $Å^{-1}$. When vacant layer sites are covered above or below with interlayer cations, as in the hexagonal birnessite (HBi, $Mn^{2+}_{0.05}Mn^{3+}_{0.12}(Mn^{4+}_{0.74}Mn^{3+}_{0.10}\square_{0.17})O_{1.7}(OH)_{0.3}$, where □ represents vacancies; Drits, et. al., 1997; Silvester et al., 1997), a shoulder appears on the steeply rising left side of this oscillation (Fig. 16c). Using this spectral feature, and a thorough analysis of EXAFS data into the *R* space after Fourier transformation, we found that the unknown soil sample has about as many corner-sharing metal polyhedra in the interlayers as there are in HBi (i.e., 17 %). However, the method is insensitive to the nature (i.e., Zn vs. Mn) and proportion of cationic species in the interlayers. The third indicator region ranges over the 7.5-10 $Å^{-1}$ interval and is sensitive to the amount and ordering of $Mn^{3+}$ in the manganese layer. When the amount of $Mn^{3+}$ in the layer is nil or low, as in synthetic turbostratic birnessite (dBi, $\delta\text{-}H_{4y}Na_{4x}(Mn^{4+}_{1-x-y}\square_{x+y})O_2 \cdot zH_2O$; Villalobos et al., 2003), the two resonances observed in this spectral region peak at 8.05 and 9.2 $Å^{-1}$ (Fig. 16d). When the amount of layer $Mn^{3+}$ is high, the two resonances either shift to 7.9 and 9.0 $Å^{-1}$, as in lithiophorite, or the first resonance splits into two maxima at 7.8 and

8.1 $Å^{-1}$ and the second shifts to 8.9 $Å^{-1}$, as in TcBi (Fig. 16a,b). The leftward shift in frequency again indicates higher interatomic distances, and is consistent with the bigger size of $Mn^{3+}$ relative to $Mn^{4+}$. The split of the first resonance arises from the segregation of the $Mn^{3+}$ cations in rows along the [010] direction in TcBi (Drits et al., 1997; Lanson et al., 2000b). Using this spectral region as a fingerprint for the stoichiometry of the manganese layer, we confirmed that the unknown soil birnessite has no detectable $Mn^{3+}$. We conclude that the turbostratic birnessite at POI-2 has a generic soil birnessite structure with no detectable $Mn^{3+}$ but with metal species in the interlayer region forming tridentate surface complexes above vacant layer Mn sites. Consequently, there is no obvious structural hindrance to the sorption of Zn on this birnessite species. Reasons for the mixture of Zn species at this spot should be sought in the biogeochemical complexity of the upper soil and the lack of geochemical equilibrium after 27 months of Zn migration.

The P-EXAFS spectrum of the <0.2 μm fraction from the contaminated soil (sample Fine_Cont_SSF) exhibits a weak, but significant, angular dependence (Fig. 17a). Comparison of the α=35 spectra from the two soil samples shows that they bear strong resemblance (Fig. 17b). A difference in shape is observed at 7-8 $Å^{-1}$, but it may not be significant given the higher noise level of the third oscillation. Similarly to the uncontaminated soil sample, a reasonably good, though not perfect, spectral agreement was obtained assuming a single phyllosilicate species. The spectral match improved upon adding Zn-sorbed ferrihydrite (ZnFh) to the fit. The mixed Zn speciation in the contaminated soil sample accounts for the weaker angular dependence of its P-EXAFS spectrum relative to the uncontaminated soil sample (Fig. 8a). Figure 18 shows that other possible layered mineral species (e.g., hydrotalcite and hydroxy-Al) gave poor matches to the spectrum from the contaminated soil.

As many as five firm Zn species, sphalerite, franklinite, gahnite-franklinite mixture or solid-solution, Zn-goethite, and Zn-phyllosilicate, and one possible species, Zn-birnessite, were identified in the contaminated soil. Sphalerite, franklinite and gahnite were not detected in the native soil and clearly are anthropogenic species, which migrated downwards from the overlying sediment in the course of the 27 months of deposition. The extent of contamination was evaluated by determining the fractional amount of each Zn species from the powder EXAFS spectrum of the <50 μm fraction (sample Coarse_Cont). The <50 μm and <0.2 μm powder spectra bear no resemblance (Fig. 19a), which means that the Zn-phyllosilicate component is not predominant in the bulk sample. This contrasts with the uncontaminated soil for which the <50 μm and <0.2 μm spectra were almost identical and dominated by the Zn-phyllosilicate species. The best one-component spectral fit of the <50 μm fraction was obtained with 80 % ZnS (*Res* = 0.22, Fig. 19b). This simulation reproduced well the spectral phase, but not the wave envelope, justifying the addition of a second component species to the fit. The best two-component fit was obtained with 66% ZnS + 49% Zn-substituted α-FeOOH (*Res* = 0.075, Fig. 19c). This second species was identified by μ-EXAFS in the native soil, but it is doubtful that it comprises half of the total Zn on the basis of μ-XRD, which indicated that goethite is relatively seldom present. Ferrihydrite, which is the predominant secondary Zn-containing species in the sediment, would be a more realistic Fe (oxyhydr)oxide species than goethite. Replacing goethite by ferrihydrite in the spectral fit shifted the first oscillation of the reconstructed spectrum to higher *k* values (Fig. 19d). Since the frequency of this oscillation

depends on the metal-oxygen distance, and Zn is fully tetrahedral on ferrihydrite (Waychunas et al., 2002; Trivedi et al., 2004), the misfit in frequency suggests that Zn is octahedrally coordinated in the unknown second species. This interpretation explains why goethite was statistically preferred to ferrihydrite in the two-component fit because Zn is octahedral when it is sorbed or incorporated into the goethite structure (Schlegel et al., 1997). As Zn is also six-fold coordinated in phyllosilicate, which is overwhelmingly present in the native soil, and in the <0.2 μm sub-fraction of the Coarse_Cont sample, a three-component fit was attempted. The optimum agreement was obtained with a mixture of sphalerite (~63 ± 10 %), ferrihydrite (~29 ± 10 %) and phyllosilicate (~25 ± 10 %, *Res* = 0.060); the assumption of goethite instead of ferrihydrite yielded a poorer match (*Res* = 0.073) (Fig. 19e,f). This spectral decomposition into three components is more reasonable as it is collectively consistent with all the other data, such as the low abundance of goethite relative to poorly-crystalline Fe (oxyhydr)oxides revealed by μ-XRD, the abundance of Zn-ferrihydrite in the sediment (Isaure et al., 2002), and the predominance of Zn-phyllosilicate in the <0.2 μm fraction of the contaminated soil.

## 4. DISCUSSION

**4.1 Solid-state speciation of Zn in the uncontaminated soil.** Despite the low concentration of Zn in the native soil (45 mg $kg^{-1}$), and the heterogeneity and complexity of this natural matrix, the synergetic use of microanalytical (μ-SXRF) and microstructural (μ-XRD, μ-EXAFS) techniques allowed us to identify with a high degree of precision the nature of mineral species hosting Zn. Zn was partitioned between three coexisting minerals: zincochromite, phyllomanganate, and phyllosilicate. No gradient in abundance of any phase was observed in the upper 20 cm of the soil. In uncontaminated soils, one or two species often dominate, outnumbering other species by one to several orders of magnitude (Manceau et al., 2004). Determining the fractional amount of each individual species is important to bridge micrometer-scale and macroscopic observations aiming to predict the fate of metals in the environment. Application of powder EXAFS spectroscopy to the bulk soil indicated that Zn is largely associated with phyllosilicate, and that the two other species contained less than 10 % of the total Zn. The possible origin and occurrence of these three species are discussed next.

In industrialized countries, truly pristine ecosystems no longer exist, and one may question whether zincochromite is a natural species or a by-product of the Zn smelter located at about 10 km from the sampling site. The mineralogy of materials formed during the smelting of ZnS has been catalogued by Thiry et al. (2002). Many Zn-bearing phases were identified in this survey, including willemite ($Zn_2SiO_4$), hemimorphite ($Zn_4Si_2O_7(OH)_2{\cdot}H_2O$), hardystonite ($Ca_2ZnSi_2O_7$), franklinite ($ZnFe_2O_4$), gahnite ($ZnAl_2O_4$), zincite (ZnO), gunningite ($ZnSO_4{\cdot}H_2O$), serpierite ($Ca(Cu,Zn)_4(SO_4)_2(OH)_6{\cdot}3H_2O$), smithsonite ($ZnCO_3$), hydrozincite ($Zn_5(CO_3)_2(OH)_6$), but not zincochromite ($ZnCr_2O_4$). To our knowledge, this zinc spinel has never been identified in contaminated soils. The absence of zincochromite in non-ferrous metallurgical Zn tailings is consistent with the geochemistry of chromium since this element does not substitute for Zn and Pb in sulfide ores, but rather precipitates as chromatite ($FeCr_2O_4$)

in mafic magmatic intrusions. Therefore, zincochromite is unlikely to be a refractory waste product from Zn smelters. In contrast, this mineral was identified recently at 80-130 cm depth in the fragipan (Btx) horizon of an Aeric Fragiaquult soil, and this species was clearly natural (Manceau et al., 2004). Since spinels are sparingly soluble, they are resistant to weathering and are often found in Earth's surface formations. Consequently, we consider that the zincochromite grains observed in the studied soil are remnant minerals inherited from the parent rock.

$^{IV}$Zn-sorbed birnessite is a common natural species often encountered in soil ferromanganese coatings and concretions (Manceau et al., 2000a, 2002a, 2003). The affinity of zinc for manganese precipitates is confirmed in this study, and by reference to other natural occurrences it can be inferred that this Zn species results from pedogenic differentiation. Recently, this species was also found in a banded ferromanganese nodule from the Mecklenburg Bight of the SW Baltic Sea (Marcus et al., 2004). The outer Mn layers of the nodules from this area were steadily enriched in Zn relative to the inner layers as a result of increasing marine pollution in recent years. Consequently, the fraction of Zn bound to birnessite may be anthropogenic since the whole area has been exposed to smelting activities for about a century and diffuse Zn pollution of the local environment undoubtedly occurred (Sobanska, 1999).

Many recent speciation studies support the conclusion that Zn-phyllosilicate is the most common and abundant zinc mineral form in steady-state soils in temperate climates (Manceau et al., 2000a, 2004; Scheinost et al., 2002; Juillot et al., 2003). The present study provides new support for this finding since zinc-containing phyllosilicate makes up the main zinc component in the <50 μm fraction of the native soil and this fraction contains ~100 % of total zinc. The occurrence of this finely divided species in the 0.2 μm to 50 μm fraction can be explained by the formation of clay coatings on mineral grains or aggregates.

In acidic clayey soils, zinc predominantly forms outer-sphere complexes in the interlayer region of phyllosilicates or can be sorbed or incorporated in hydroxy-Al interlayers (Scheinost et al., 2002). At neutral to alkaline pH, hydroxy-Al phyllosilicates and outer-sphere complexes seem to be relatively unstable, and zinc hydrolysis promotes its bonding to phyllosilicate layers through inner-sphere complexation to sorbent metal cations at layer edges or in the bulk (Mc Bride, 1994). Although considerable knowledge exists on the molecular mechanism of metal sorption on phyllosilicates, the immense majority of studies were conducted on laboratory systems, and data on the crystal chemical status of trace metals in general, and zinc in particular, in natural hydrous silicates is lacking. Determining whether zinc is sorbed on layer edges or is in substitutional position within the phyllosilicate structure, and if the substrate has a dioctahedral or trioctahedral structure, is important from mineralogical, geochemical, and environmental standpoints. Earlier works showed that powder EXAFS spectroscopy has little sensitivity to the dioctahedral versus trioctahedral local structural environment of octahedrally coordinated metal cations in sheet silicates (Manceau, 1990). Recent progress in the development of polarized EXAFS spectroscopy and multiple-scattering theory for the analysis of higher shell contributions, established that the two local structures could be distinguished by thorough analysis of specific atomic shells, whose symmetry is broken in dioctahedral layer silicates owing to the presence of vacant octahedral sites. The most diagnostic atomic shells are (1) the first (Tet1) and second (Tet2) Si shells, which are split in dioctahedral (Tsipursky et al., 1984) but not in trioctahedral layer silicates (Rayner and Brown, 1973), (2) basal oxygens at about 4.1-4.2 Å (O4 shell, Fig. 9b), which are detected in trioctahedral layer silicates by

orienting the electric field vector perpendicularly to the layer plane (Manceau et al., 1998), and (3) the third metal shell at 6.0-6.2 Å (Oct3), which is intense in trioctahedral layers due to multiple-scattering effects, but weak in dioctahedral layers (O'Day et al., 1994; Manceau et al., 2000b).

The previous characteristics are illustrated in Figure 20a with the polarized radial structure functions of the Redhill montmorillonite obtained by Fourier transforming the P-EXAFS spectra presented in Figure 8c. In the out-of-plane orientation of the electric field vector ($\alpha$ = 90°), the second (Tet1) peak is clearly asymmetrical and the third (Tet2) peak broadened as a result of the split of the Zn-Si distances in the successive Si shells and the increase of this split with the radial distance from the central atom. The dioctahedral character of the Zn environment is also attested by the absence of the dichroic peak from basal oxygens located between the Tet1 and Tet2 peaks in trioctahedral sheet silicates (see e.g., Fig. 16 in Manceau et al., 1998, and Fig. 10 in Manceau et al., 2000b). Finally, the absence of a multiple-scattering Al3 peak at twice the Zn-Al1 distance in the parallel orientation ($\alpha$ = 10°) indicates that either the Al3 or Al2 positions are vacant, since in the former case there is no Al atom at this distance and in the latter no focusing effect occurs (Manceau et al., 2000b).

The four shells discussed previously (Tet1, Tet2, O3, and Oct3) ought to modify the overall shape and frequency of the EXAFS spectrum whenever the local structure has a dioctahedral or trioctahedral character because they are for different atoms (Si, O, Al or Mg) at different radial distances from the central X-ray absorber. Although these spectral perturbations are small, they collectively modify the shape of the EXAFS spectrum even at room temperature as shown in Figure 20b for diluted Zn in montmorillonite (Redhill) and kerolite (ZnKer003, $Si_4(Zn_{0.03}Mg_{2.97})O_{10}(OH)_2.nH_2O$).

Comparing EXAFS spectra for natural soil samples and the models, we found that none of the reference spectra, in which Zn is incorporated either in a dioctahedral or trioctahedral sheet, satisfactorily accounted for experimental data. Instead, fair spectral agreement was obtained with Zn-sorbed on the trioctahedral reference, hectorite. Study in progress shows that Zn forms a distinctive inner-sphere surface complex on montmorillonite. Consistently, Dähn et al. (2003) showed that the dioctahedral character of the bulk structure of montmorillonite is preserved at the mineral surface and can be detected by sorbing a metal on layer edges. All these data collectively suggest that zinc is most likely sorbed at the surface of phyllosilicate in the soils from this region, and that its local environment has a trioctahedral character. This interpretation is different from that proposed by Juillot et al. (2003), who contended that Zn is incorporated in the octahedral sheet of dioctahedral phyllosilicate (namely montmorillonite) in soils from the same region. In their study, the dioctahedral versus trioctahedral character of the Zn local structure was differentiated from the number of Oct1 ($N_{Mg/Al}$) to Tet1 ($N_{Si}$) nearest neighbors ($N_{Mg/Al}/N_{Si}$=0.5) calculated from the spectral simulation of $HNO_3$-treated samples' data. The use of this ratio for discriminating the two types of local structures is equivocal because it is about ½ (actually 3/4) whenever Zn is incorporated in the structure of montmorillonite, but also when Zn is sorbed on the surface of a trioctahedral phyllosilicate due to the breaking of the lattice at the mineral surface (Schlegel et al., 2001). As shown previously, the dioctahedral versus trioctahedral structural trait is more rigorously determined from analysis of the whole EXAFS spectra, since they include single and multiple scattering contributions from diagnostic distant shells, rather than by Fourier filtering a set of unknown and essentially non-diagnostic

atomic shells and performing multiple-parameter spectral fits. As discussed in Manceau et al. (2002a) and O'Day et al. (2004), there are some concerns about the uniqueness of the structural interpretation when complex EXAFS spectra from individual or a mix of species are broken up into shells, especially when only one or two shells are analyzed quantitatively, thus limiting the structural analysis to ca. 2-3.5 Å. Also, acidic treatment of samples should be avoided because the formation and stability of inner-sphere surface complexes are pH-dependent (McBride, 1994; Stumm and Morgan, 1996).

**4.2 Solid-state speciation and origin of Zn in the contaminated soil.** Zn concentration in the <50 μm fraction of the topsoil (0-10 cm depth) increased from 61 mg $kg^{-1}$ to 269 mg $kg^{-1}$ after 15 months of deposition. Anthropogenic Zn in this layer amounts to ~ 0.8 % of total Zn initially present in the sediment. If one includes the pool of Zn which migrated to the 10-20 cm layer, this percentage rises to 1.2 %, that is ~4 kg Zn over an area of 50 $m^2$. This quantity corresponds approximately to the total amount of Zn leached from the sediment because the Zn concentration did not increase significantly below 20 cm, and neither was it detected in ground water. Three new Zn species were detected in the contaminated soil: sphalerite (ZnS), franklinite ($ZnFe_2O_4$) and Zn bound to poorly crystalline Fe (oxyhydr)oxides. The two first species undoubtedly result from the gravitational transfer of minute grains from the sediment to the underlying soil. Although authigenic formation of ZnS can occur in submerged soils and sediments (Peltier et al., 2003), ZnS precipitation is unlikely here because the reduction of oxygenated to sulfide Zn forms during flooding periods occurs at Eh < -100 mV (Bostick et al., 2001) and the Eh value in the lixiviates did not decrease below +50 mV. Also, the particle morphology and size in the sediment and soil were the same. Since ZnS makes up 73 ± 10 % of total Zn in the sediment, and ~63 ± 10 % in the first 0-10 cm layer of the soil, ZnS particulate transfer is the predominant mechanism of Zn propagation into the local environment. Franklinite was a minor species in the sediment, since this species was detected by μ-EXAFS but not bulk EXAFS spectroscopy (Panfili et al., 2005) and, consequently, still is in the contaminated soil (<5 % total Zn). Zn-ferrihydrite is the second most abundant Zn species together with Zn-phyllosilicate in the 0-10cm soil layer, making up the remaining 40 % of the total Zn. Zn-ferrihydrite was shown to result from the weathering of ZnS and $FeS_2$ grains in oxidizing environment (Hesterberg et al., 1997; O'Day et al., 1998; Hochella et al., 1999; Webb et al., 2000, Bostick et al., 2001, Carroll et al., 2002; Jeong et al., 2003), and represents the main neoformed Zn species in both the overlying sediment (Isaure et al., 2002) and the upper soil. Precipitation of Zn-ferrihydrite at the surface of (Fe,Zn)S coarse grains (ZnS contains up to 20 % substitutional Fe, Thiry et al., 2002) was revealed by micro-PIXE and micro-EXAFS (Isaure et al., 2002), and the formation of this finely divided surface precipitate on incompletely oxidized (Fe,Zn)S remnant grains accounts for the detection of this secondary species in the <50 μm coarse fraction. Contamination of the underlying soil by physical transport of Zn-ferrihydrite as colloids or surface coatings on primary grains is likely, and this enrichment mechanism probably adds to the in-situ formation of this species by the oxidation of sulfide particles in the oxygenated soil environment. More generally, the dim reddish-brown cast in the RGB representation of the argillaceous matrix beneath the sediment-soil interface, and the vertical gradient in Zn concentration indicate that the fine soil matrix has been permeated with zinc solubilized by the oxidative dissolution of ZnS particles from the sediment.

**4.3 Environmental implications.** This study shows that Zn is released from the sediment to percolating water during the non-flooding summer periods because of the oxidative dissolution of Zn sulfides. In contrast, Zn is essentially immobile during the flooding periods. The oxidation of zinc and iron sulfides is probably enhanced by bacterial activity since sulfato-oxidizing bacteria (*Thiobacillus thiooxidans* and *thiobacillus ferrooxidans*) were identified in the sediment and were found to increase the release of metals in a laboratory study (Lors et al., 2001). Pot experiments in greenhouses showed that the colonization of the dredged sediment by plants increased the oxidation rate of metal sulfides, and that ZnS was completely dissolved after two years of vegetation (Panfili et al., 2005). This companion study also showed that Zn released in solution was immobilized in-situ as Zn-phosphate, a weakly soluble species, by adding phosphorous amendments to the sediment. However, the long-term stability of this phosphate phase is unknown, and the present study demonstrates that Zn may contaminate the local environment if no precautions are taken to restrict its mobility. Collecting the solutions containing the dissolved contaminants is preferable to in-situ immobilization as a way to remediate the site because there is always a risk of the resupply of metal from sequestering phases if the physico-chemical conditions of the deposit are modified over time. For example, acidification of the sediment or excretion of organic acids by plants, such as citrate, may increase the solubility and bioavailability of Zn in the treated sediment (Kirpichtchikova et al., 2003), in contrast to Pb, which is more durably immobilized by the addition of phosphate (Ryan et al., 2004).

*Acknowledgment* - The ALS and the CNRS, which supports the French-CRG program at ESRF, are acknowledged for the provision of beamtime. O. Proux and J.L. Hazemann are thanked for their assistance during EXAFS measurements on FAME (ESRF). Preliminary SEM-EDS measurements were performed at the LESTS laboratory of the CEA/IRSN in Fontenay-aux-Roses, France. This research was supported by European FEDER funds, by the Director, Office of Energy Research, Office of Basic Energy Sciences, Materials Sciences Division of the U.S. Department of Energy, under Contract No. DE-AC03-76SF00098.

## REFERENCES


Ankudinov A.L., Ravel B., Rehr J.J. and Conradson S.D. (1998) Real-space multiple scattering calculation of XANES, *Phys. Rev.* **B58**, 7565-7576.

Baize D. (1997) *Teneurs totales en éléments traces métalliques dans les sols*. Institut National de la Recherche Agronomique (INRA) Editions.

Bostick B.C., Hansel C.M., La Force M.J. and Fendorf S. (2001) Seasonal fluctuations in zinc speciation within a contaminated wetland. *Environ. Sci. Technol.* **35**, 3823-3829.

Carroll S., O'Day P.A., Esser B. and Randall S. (2002) Speciation and fate of trace metals in estuarine sediments under reduced and oxidized conditions, Seaplane Lagoon, Alameda Naval Air Station (USA). *Geochem. Trans.* **3**, 81-101.

Cotter-Howells J.D., Champness P.E., Charnock J.M. and Pattrick R.A.D. (1994) Identification of pyromorphite in mine-waste contaminated soils by ATEM and EXAFS. *Europ. J. Soil Sci.* **45**, 393-402.

Dähn R., Scheidegger A. M., Manceau A., Schlegel M. L., Baeyens B., Bradbury M. H. and Chateigner D. (2003) Structural evidence for the sorption of metal ion on the edges of montmorillonite layers. A polarized EXAFS study. *Geochim. Cosmochim. Acta* **67**, 1-15.

Drits V.A., Silvester E., Manceau A. and Gorskhov A.I.(1997) The structure of monoclinic Na-exchanged birnessite and hexagonal H-birnessite. Part 1. Results from X-ray diffraction and selected area electron diffraction. *Am. Mineral.* **82**, 946-961.

Gaillot A. C., Flot D., Drits V. A., Burghammer M., Manceau A. and Lanson B. (2003) Structure of synthetic K-rich birnessites obtained by high-temperature decomposition of KMnO4. I. Two-layer polytype from a 800°C experiment. *Chem. Mater*. **15**, 4666-4678.

Hansel C. M., Fendorf S., Sutton S. and Newville M. (2001) Characterization of Fe plaque and associated metals on the roots of mine-waste impacted aquatic plants. *Environ. Sci. Technol.* **35**, 3863-3868.

Hesterberg D., Sayers D. E., Zhou W., Plummer G. M. and Robarge W. P. (1997) X-ray absorption spectroscopy of lead and zinc speciation in a contaminated groundwater aquifer. *Environ. Sci. Technol.* **31**, 2840-2846.

Hochella M.F., Moore J.N., Golla U. and Putnis A. (1999) A TEM study of samples from acid mine drainage systems: Metal-mineral association with implications for transport. *Geochim. Cosmochim. Acta* **63**, 3395-3006.

Isaure M.P., Laboudigue A., Manceau A., Sarret G. and Tiffreau C. (2002) Quantitative Zn speciation in a contaminated dredged sediment by µ-PIXE, µ-SXRF, EXAFS spectroscopy and Principal component analysis. *Geochim. Cosmochim. Acta* **66**, 1549-1567.

Jeong G.Y. and Lee B.Y. (2003) Secondary mineralogy and microtextures of weathered sulfides and manganoan carbonates in mine waste-rock dumps, with implications for heavy-metal fixation. *Am. Mineral.* **88**, 1933-1942.

Juillot F., Morin G., Ildefonse P., Trainor T.P., Benedetti M., Galoisy L., Calas G. and Brown Jr G.E. (2003) Occurrence of Zn/Al hydrotalcite in smelter-impacted soils from northern France: evidence from EXAFS spectroscopy and chemical extractions. *Am. Mineral.* **88**, 509-526.

Kim C. S., Bloom N. S., Rytuba J. J. and Brown G. E. (2003) Mercury speciation by X-ray absorption fine structure spectroscopy and sequential chemical extractions: A comparison of speciation methods. *Environ. Sci. Technol.* **37**, 5102-5108.

Kirpichtchikova T., Manceau A., Lanson B., Sarret G., Marcus M. A. and Jacquet T. (2003) Speciation and mobility of heavy metals (Zn, Cu and Pb) in soil contaminated by sewage irrigation. *J. Phys. IV* **107**, 695-698.

Kneebone P. E., O'Day P. A., Jones N. and Hering J. G. (2002) Deposition and fate of arsenic in iron- and arsenic-enriched reservoir sediments. *Environ. Sci. Technol.* **36**, 381-386.

Lanson B., Drits V.A., Gaillot A.C., Silvester E., Plancon A. and Manceau A. (2002a) Structure of heavy-metal sorbed birnessite. Part 1. Results from X-ray diffraction. *Am. Mineral.* **87**, 1631-1645.

Lanson B., Drits V.A., Fen Q. and Manceau A. (2002b) Crystal structure of synthetic Na-rich birnessite: Evidence for a triclinic one-layer cell. *Am. Mineral.* **87**, 1662-1671.

Lors C., Tiffreau C. and Laboudigue A. (2001) Effect of microbial activities on the leaching of heavy metals from contaminated sediments. In *Proceedings of the 9th International Symposium on Microbial Ecology*, 26-31 August 2001, Amsterdam, The Netherlands p.330.

Manceau A. (1990) Distribution of cations among the octahedra of phyllosilicates: insight from EXAFS. *Can. Mineral.* **28**, 321-328.

Manceau A., Bonnin D., Kaiser P. and Frétigny C. (1988) Polarized EXAFS of biotite and chlorite. *Phys. Chem. Minerals* **16**, 180-185.

Manceau A., Boisset M. C., Sarret G., Hazemann J. L., Mench M., Cambier P. and Prost R. (1996) Direct determination of lead speciation in contaminated soils by EXAFS spectroscopy. *Environ. Sci. Technol.* **30**, 1540-1552.

Manceau A., Drits V. A., Silvester E., Bartoli C. and Lanson B. (1997) Structural mechanism of Co(II) oxidation by the phyllomanganate, Na-buserite. *Am. Mineral.* **82**, 1150-1175.

Manceau A., Chateigner D. and Gates W.P. (1998) Polarized EXAFS, distance-valence least-squares modeling (DVLS), and quantitative texture analysis approaches to the structural refinement of Garfield nontronite. *Phys. Chem. Minerals* **25**, 347-365.

Manceau A., Lanson B., Schlegel M. L., Hargé J. C., Musso M., Eybert-Bérard L., Hazemann J. L., Chateigner D. and Lamble G. M. (2000a) Quantitative Zn speciation in smelter-contaminated soils by EXAFS spectroscopy. *Am. J. Sci.* **300**, 289-343.

Manceau A., Drits V.A., Lanson B., Chateigner D., Wu J., Huo D., Gates W.P. and Stucki, J.W. (2000b) Oxidation-reduction mechanism of iron in dioctahedral smectites. 2. Structural chemistry of reduced Garfield nontronite. *Am. Mineral.* **85**, 153-172.

Manceau A., Marcus M.A. and Tamura N. (2002a) Quantitative speciation of heavy metals in soils and sediments by synchrotron x-ray techniques. In *Reviews in Mineralogy and Geochemistry Vol. 49: Applications of Synchrotron Radiation in Low-Temperature Geochemistry and Environmental Science* (eds. P. Fenter, M. Rivers, N.C. Sturchio and S. Sutton). Mineralogical Society of America, Washington, DC. pp. 341-428.

Manceau A., Tamura N., Marcus M.A., MacDowell A.A., Celestre R.S., Sublett R.E., Sposito G. and Padmore H.A. (2002b) Deciphering Ni sequestration in soil ferromanganese nodules by combining X-ray fluorescence, absorption, and diffraction at micrometer scales of resolution. *Am. Mineral.* **87**, 1494-1499.

Manceau A., Lanson B. and Drits V.A. (2002c) Structure of heavy metal sorbed birnessite. Part III. Results from powder and polarized extended x-ray fine structure spectroscopy. *Geochim. Cosmochim. Acta* **66**, 2639-2663.

Manceau A., Tamura N., Celestre R.S., MacDowell A.A., Geoffroy N., Sposito G. and Padmore H.A. (2003) Molecular-scale speciation of Zn and Ni in soil ferromanganese nodules from loess soils of the Mississippi Basin. *Environ. Sci. Technol.* **37**, 75-80.

Manceau A., Marcus M.A., Tamura N., Proux O., Geoffroy N. and Lanson B. (2004) Natural speciation of Zn at the micrometer scale in a clayey soil using X-ray fluorescence, absorption, and diffraction. *Geochim. Cosmochim. Acta* **68**, 2467-2483

Marcus M.A., Manceau A. and Kersten M. (2004) Mn, Fe, Zn and As speciation in a fast-growing ferromanganese marine nodule. *Geochim. Cosmochim. Acta* **68**, 3125-3136.

Marcus M., MacDowell A.A., Celestre R., Manceau A., Miller T., Padmore H.A., Sublett R.E. (2004) Beamline 10.3.2 at ALS: a hard X-ray microprobe for environmental and materials sciences. *J. Synch. Rad*. **11**, 239–247.

McBride M.B. (1994) *Environmental Chemistry of Soils*. Oxford University Press, New York.

Morin G., Juillot F., Ostergren J.D., Ildefonse P., Calas G. and Brown Jr G.E. (1999) XAFS determination of the chemical form of lead in smelter-contaminated soils and mine tailings: Importance of adsorption process. *Am. Mineral.* **84**, 420-434.

Morin G., Juillot F., Ildefonse P., Calas G., Samama J.C., Chevallier P. and Brown Jr G.E. (2001) Mineralogy of lead in a soil developed on a Pb-mineralized sandstone (Largentière, France). *Am. Mineral.* **86**, 92-104.

Nesterov A. R. and Rumyantseva Y. V. (1987) Zincochromite $ZnCr_2O_4$ - A new mineral from Karelia [in Russian]. Zapiski Vses. Mineralog. Obshch 116, 367-371. *Am. Mineral*. **73**, 931-932.

O'Day P. A., Rehr J. J., Zabinsky S. I., and Brown G. E., Jr. (1994) Extended x-ray absorption fine structure (EXAFS) analysis of disorder and multiple-scattering in complex crystalline solids. *J. Amer. Chem. Soc.* **116**, 2938-2949.

O'Day P. A., Carroll S. A. and Waychunas G. A. (1998) Rock-water interactions controlling zinc, cadmium, and lead concentrations in surface waters and sediments, US Tri-State Mining District. 1 : Molecular identification using X-ray absorption spectroscopy. *Environ. Sci. Technol.* **32**, 943-955.

O'Day P. A., Carroll S. A., Randall S., Martinelli R. E., Anderson S. L., Jelinski J. and Knezovich J. P. (2000) Metal speciation and bioavailability in contaminated estuary sediments, Alameda Naval Air Station, California. *Environ. Sci. Technol.* **34**, 3665-3673.

O'Day P. A., Rivera N., Root R. and Carroll S. A. (2004) X-ray absorption spectroscopic study of Fe reference compounds for the analysis of natural sediments. *Am. Miner.* **89**, 572-585.

Ostergren J. D., Brown Jr G. E., Parks G. A., and Tingle T. N. (1999) Quantitative speciation of lead in selected mine tailings from Leadville, CO. *Environ. Sci. Technol.* **33**, 1627-1636.

Paktunc D., Foster A., Heald S. and Laflamme G. (2004) Speciation and characterization of arsenic in gold ores and cyanidation tailings using X-ray absorption spectroscopy. *Geochim. Cosmochim. Acta* **68**, 969-983.

Panfili F., Manceau A., Sarret G., Spadini L., Kirpichtchikova T., Bert V., Laboudigue A., Marcus M., Ahamdach N. and Libert M.F. (2005) The effect of phytostabilization on Zn speciation in a dredged contaminated sediment using scanning electron microscopy, X-ray

fluorescence, EXAFS spectroscopy and principal components analysis. *Geochim. Cosmochim. Acta*, accepted pending minor revisions.

Peltier E. F., Webb S. M. and Gaillard J. F. (2003) Zinc and lead sequestration in an impacted wetland system. *Adv. Environ. Research* **8**, 103-112.

Rayner J. H. and Brown G. (1973) The crystal structure of talc. *Clays Clay Miner*. **21**, 103-114.

Roberts D.R., Scheinost A.C. and Sparks D.L. (2002) Zinc speciation in a smelter-contaminated soil profile using bulk and microspectroscopic techniques. *Environ. Sci. Technol.* **36**, 1742-1750.

Ryan J.A., Scheckel K.G., Berti W.R., Brown S.L., Casteel S.W., Chaney R.L., Hallfrisch J., Doolan M., Grevatt P., Maddaloni M. and Mosby D. (2004) Reducing children's risk from lead in soil. *Environ. Sci. Technol.* **38**, 18A-24A.

Sarret G., Balesdent J., Bouziri L., Garnier J. M., Marcus M. A., Geoffroy N., Panfili F. and Manceau A. (2004) Zn speciation in the organic horizon of a contaminated soil by micro X-ray fluorescence, micro and powder EXAFS spectroscopy and isotopic dilution. *Environ. Sci. Technol.* **38**, 2792-2801.

Scheinost A.C., Kretzschmar R., Pfister S. and Roberts D.R. (2002) Combining selective sequential extractions, x-ray spectroscopy, and principal component analysis for quantitative zinc speciation in soil. *Environ. Sci. Technol.* **36** 5021-5028.

Schlegel M.L., Manceau A. and Charlet L. (1997) EXAFS study of Zn and ZnEDTA sorption at the goethite (alpha-FeOOH)/water interface. *J. Phys. IV* **7**, 823-284.

Schlegel M., Manceau A., Chateigner, D. and Charlet, L. (1999) Sorption of metal ions on clay minerals. I. Polarized EXAFS evidence for the adsorption of Co on the edges of hectorite particles. *J. Colloid Interface Sci.* **215**, 140-158.

Schlegel M.L., Manceau A., Charlet L. and Hazemann J.L. (2001) Asorption mechanism of Zn on hectorite as a function of time, pH, and ionic strength. *Am. J. Sci.* **301**, 798-830.

Silvester E., Manceau A., and Drits V.A. (1997) The Structure of monoclinic Na-exchanged birnessite and hexagonal H-birnessite. Part 2. Results from chemical studies and EXAFS spectroscopy. *Am. Mineral*. **82**, 962-978.

Singh B. and Gilkes R. J. (1996) Nature and properties of iron rich glaebules and mottles from some south-west Australian soils. *Geoderma* **71**, 95-120.

Sobanska S., Ricq N., Laboudigue A., Guillermo R., Brémard C., Laureyns J., Merlin J. C. and Wignacourt J. P. (1999) Microchemical investigations of dust emitted by a lead smelter. *Environ. Sci. Technol.* **33**, 1334-1339.

Sobanska S. (1999) Etude de la spéciation du plomb et du zinc dans des poussières industrielles et dans un sol contaminé. Ph.D. thesis, Université des Sciences et Technologies de Lille.

Strawn D., Doner H., Zavarin M. and McHugo S. (2002) Microscale investigation into the geochemistry of arsenic, selenium and iron in soil developed in pyritic shale materials. Geoderma **108**, 237-257.

Stumm W. and Morgan J.J. (1996) *Aquatic chemistry : chemical equilibria and rates in natural waters*. 3rd ed. John Wiley & Sons, New York.

Takahashi Y., Minamikawa R., Hattori K. H., Kurishima K., Kihou N. and Yuita K. (2004) Arsenic behavior in paddy fields during the cycle of flooded and non-flooded periods. *Environ. Sci. Technol.* **38**, 1038-1044.

Teo B.K. (1986) *EXAFS: Basic Principles and Data Analysis*. Springer, Berlin.

Thiry M., Huet-Taillanter S. and Schmitt J. M. (2002) La friche industrielle de Mortagne-du-Nord (59) - I - Prospection du site, composition des scories, hydrochimie, hydrologie et estimation des flux. *Bull. Soc. Géol. France* **173**, 369-381.

Tack F.M.G., Singh S.P. and Verloo M.G. (1999) Leaching behaviour of Cd, Cu, Pb and Zn in surface soils derived from dredged sediments. *Environ. Pollution* **106**, 107-114.

Trivedi P., Dyer J.A., Sparks D.L. and Pandya K. (2004) Mechanistic and thermodynamic interpretations of zinc sorption onto ferrihydrite. *J. Colloid Interface Sci.* **270**, 77-85.

Tsipursky S. I. and Drits V. A. (1984) The distribution of cations in the 2:1 layers of dioctahedral smectites studied by oblique-texture electron diffraction. *Clay Miner.* **19**, 177-193.

Waychunas G.A., Fuller C.C. and Davis J.A. (2002) Surface complexation and precipitate geometry for aqueous Zn(II) sorption on ferrihydrite I: X-ray absorption extended fine structure spectroscopy analysis. *Geochim. Cosmochim. Acta* **66**, 1119-1137.

Vandecasteele B., De Vos B. and Tack F. M. G. (2002) Heavy metal contents in surface soils along the Upper Scheldt river (Belgium) affected by historical upland disposal of dredged materials. *Science Tot. Environ.* **290**, 1-14.

Villalobos M., Toner, B., Bargar, J. and Sposito G. (2003) Characterization of the manganese oxide produced by *Pseudomonas putida* strain MnB1. *Geochim. Cosmochim. Acta* **67**, 2649-2662.

Webb S.M., Leppard G.G. and Gaillard J.F. (2000) Zinc speciation in a contaminated aquatic environment: characterization of environmental particles by analytical electron microscopy. *Environ. Sci. Technol.* **34**, 1926-1933.

Yang D. S. and Wang M. K. (2003) Characterization and a fast method for synthesis of sub-micron lithiophorite. *Clays Clay Miner.* **51**, 96.

Table 1. Characterization of the initial uncontaminated soil (0-20 cm)

| Size fraction (µm) | 2000 to 500 | 500 to 200 | 200 to 50 | 50 to 20 | 20 to 2 | <2 |
|---|---|---|---|---|---|---|
| Fractional weight (%) | 0.9 | 4.7 | 12.2 | 45.0 | 25.2 | 12.0 |
| Elemental concentrations (mg $kg^{-1}$) | | | | | | |
| Zn | 45 | | P | 610 | | |
| Pb | 20 | | K | 14800 | | |
| Cd | 0.7 | | Ca | 37600 | | |
| Na | 6800 | | Mn | 520 | | |
| Mg | 3900 | | Fe | 21200 | | |
| Al | 40600 | | | | | |
| Mineralogy | | | | | | |
| Quartz | +++ | | Kaolinite | ++ | | |
| Calcite | ++ | | Illite | +++ | | |
| Albite | ++ | | Smectite | ++ | | |
| Microcline | + | | Chlorite | + | | |

+++: High intensity of diffraction peaks, ++: medium intensity, +: low intensity.

## Figure caption

**Figure 1** : pH, Eh (a), and Zn and Fe (b) variations measured in soil water during the 18 months following the sediment deposition.

**Figure 2** : Zn concentration in the <50 µm fraction of the upper (0-10 cm) and lower (10-20 cm) soil before the sediment deposition, and after 3, 9, 12, 15 and 18 months. Zn content in the soil increased after 12 months of deposition.

**Figure 3** : Two-color (GB) (a) and tricolor (RGB) (b,c) µ-SXRF maps of the distribution of Zn (red), Fe (green), and Mn (blue) in the upper (0-10 cm) uncontaminated soil. In the (a) and (b) maps, each pixel is colored red in proportion to the Zn signal, green in proportion to Fe, and blue in proportion to Mn. In (c) the saturation level of the red channel was lowered five times ($I(Zn\text{-}K\alpha)_{Max}/5$). (d) grayscale (negative-contrast) µ-SXRF map of the distribution of Zn obtained by subtraction the normalized maps taken 50 eV above and below the Zn K-edge to eliminate the background signal. The incident X-ray energy (*E)* is 10 keV, map size: H = 2100 µm x V = 1900 µm, beam size: H = 16 µm x V = 5 µm, step size: H = 20 µm x V = 20 µm, dwell time: 400 ms/point.

**Figure 4** : µ-SXRF maps of the distribution of Zn (red), Fe (green), and Mn (blue) in the lower (10-20 cm) uncontaminated soil. Same experimental conditions and representation as in Figure 3.

**Figure 5** : One-dimensional µ-XRD patterns (λ = 2.066 Å) at Mn-rich spot (POI-2, Fig. 4c) (a), and in the clayey matrix (b). A: albite, An: analcime, At: anatase, B: birnessite, C: calcite, D: dolomite, FeOx: poorly-crystalline Fe (oxyhydr)oxide, G: goethite, I: ilmenite, M: microcline, P: phyllosilicate, Q: quartz. The relative intensity of the *hkl* reflections for the coarse grains are different from the powder pattern of the same mineral species because only a few individual crystals satisfy the Bragg condition in µ-XRD experiment. One-dimensional µ–XRD patterns are obtained from two-dimension patterns by integrating intensities at constant Bragg angle.

**Figure 6** : $k^3$-weighted Zn K-edge µ-EXAFS spectrum collected at point POI-1 in Fig. 4c together with zincochromite (a) and franklinite (b). c,d) Fourier transforms.

**Figure 7** : $k^3$-weighted Zn K-edge µ-EXAFS spectrum collected at point POI-2 in Fig. 4c together with $^{IV}$Zn-sorbed birnessite ($^{IV}$ZnBi) from Marcus et al. (2004) (a), and $^{IV/VI}$Zn-sorbed birnessite (b), in which 2/3 of Zn is tetrahedrally coordinated and 1/3 is octahedrally coordinated (ZnBi 8 reference from Manceau et al., 2002c). c,d) Fourier transforms. e,f) Structural models for Zn-sorbed birnessite in which Zn is fully tetrahedral (e) and partly tetrahedral and octahedral (f).

**Figure 8** : Polarized EXAFS spectra from the <0.2 μm fraction of the uncontaminated soil (sample Fine_Raw_SSF) (a), from a Zn-sorbed hectorite reference (sample H_30_6h_SSF from Schlegel et al., 2001) (b), and from Na-exchanged Redhill montmorillonite (c).

**Figure 9** : Structural model for the sorption of Zn on the layer edge of a trioctahedral phyllosilicate (a), and Zn for Al substitution in montmorillonite (b). The successive atomic shells around Zn are labelled.

**Figure 10** : Powder EXAFS spectra and Fourier transforms compared for the clay fraction of the uncontaminated soil (Fine_Raw_SSF $\alpha$=35°, solid line) and a series of references (dotted line): MN3 soil sample from Manceau et al. (2000a) (a,b); Zn-sorbed hectorite (sample H_30_6h_SSF, $\alpha$=35°) from Schlegel et al. (2001) (c,d); synthetic Zn-substituted kerolite (ZnKer070, $Zn_{0.7}Mg_{2.3}Si_4O_{10}(OH)_2 \cdot nH_2O$) from Schlegel et al. (2001) (e,f); Redhill montmorillonite ($\alpha$ = 35°) (g,h), and SAz-1 montmorillonite (i,j).

**Figure 11** : Powder EXAFS spectra of the <0.2 μm (Fine_Raw_SSF $\alpha$=35°, solid line) and <50 μm (Fine_Coarse, dotted line) fractions for the uncontaminated soil.

**Figure 12** : Two-color (GB) (a,c) and tricolor (RGB) (b,d) μ-SXRF maps of the distribution of Zn (red), Fe (green), and Mn (blue) in the upper (a,b) and lower (c,d) contaminated soil. The green and blue pixels are in proportion to Fe and to Mn, while the saturation level of the red pixel has been decreased four times to increase the sensibility to Zn. *E* = 10 keV, map size: H = 3240 μm x V = 4350 μm, beam size: H = 16 μm x V = 5 μm, step size: H = 20 μm x V = 20 μm, dwell time: 400 ms/point. The maps are orientated vertically relative to the soil profile.

**Figure 13** : X-ray fluorescence spectra recorded at *E* = 10 keV from points-of-interest (POIs) in the tricolor maps from the contaminated soil (Fig. 12). Spectra labelled 'POI' were recorded at the maximum of Zn K$\alpha$ intensity of the POI, while spectra labelled 'fine matrix' were recorded in the matrix a few tens of micrometers apart the POI.

**Figure 14** : μ-XRD patterns ($\lambda$ = 2.066 Å) of the contaminated soil. (a) clayey matrix, (b) Mn-rich spot (POI-2, Fig. 12b). A: albite, At: anatase, B: birnessite, C: calcite, FeOx: poorly-crystalline Fe (oxyhydr)oxide, I: ilmenite, K: kaolinite, Mu: mullite, P: phyllosilicate, Q: quartz.

**Figure 15** : Zn K-edge μ-EXAFS spectra recorded at POI-6 (a), POI-8 (b) and POI-2 (c) of the contaminated soil, and Fourier transform of the spectrum at POI-2 (d) (solid lines). The spectrum at POI-6 was best simulated (*Res* = 0.22) assuming a mixture of gahnite ($ZnAl_2O_4$) and franklinite ($ZnFe_2O_4$), in proportions of 47 % and 33 %, respectively (dotted line). The spectrum at POI-8 was best simulated with a mixture of 61 % Zn-substituted goethite ($\alpha$-FeOOH) + 37 % franklinite (*Res* = 0.14) (dotted line). Plots (c) and (d) compare experimental data at POI-2 in the contaminated soil (Fig. 12b) (solid line) and at POI-2 in the uncontaminated soil (Fig. 4c) (dotted line).

**Figure 16** : Mn K-edge μ-EXAFS spectrum at POI-2 of the contaminated soil in Fig. 12b (solid line), compared to Mn-K edge data from a series of birnessite references (dotted line). (a) lithiophorite from Yang and Wang (2003), (b) triclinic birnessite (TcBi) from Lanson et al. (2002a), (c) hexagonal birnessite (HBi) from Silvester et al. (1997), and (d) δ-$MnO_2$ (dBi) from Villalobos et al. (2003). Note the phase differences in the "staircase" region, pointed out with arrows, and the features in the "indicator" region, pointed out with thin vertical lines. The EXAFS for the sample has been multiplied by 1.5 to compensate for overabsorption.

**Figure 17** : Polarized EXAFS spectra from the <0.2 μm fraction of the contaminated upper soil (sample Fine_Cont_SSF) (a), and comparison with the spectrum from the <0.2 μm fraction of the uncontaminated soil at $\alpha = 35°$ (sample Fine_Raw_SSF) (b).

**Figure 18** : $k^3$-weighted Zn-EXAFS spectrum from the <0.2 μm fraction of the contaminated soil ($\alpha = 35°$) compared to a selection of reference compounds: Zn-Al layered double hydroxide (LDH, $Zn_2Al(OH)_6(CO_3)_{0.5}$) (a); Zn-coprecipitated hydroxy-Al interlayered montmorillonite (HIMc) (b); Zn-sorbed hydroxy-Al interlayered montmorillonite (HIMs) (c). The EXAFS data from the hydroxy-Al species are from Scheinost et al. (2002).

**Figure 19** : Zn K-edge powder EXAFS spectrum from the <50 μm fraction of the contaminated upper soil (sample Coarse_Cont), compared to the P-EXAFS spectrum ($\alpha = 35°$) from the <0.2 μm fraction of the same sample (Fine_Cont_SSF) (a), and one-, two- and three-component fits with sphalerite (ZnS), Zn-substituted goethite (α-FeOOH), Zn-sorbed ferrihydrite (ZnFh), and the <0.2 μm fraction (Fine_Cont_SSF) (b-d).

**Figure 20** : Polarized radial structure functions of the Redhill montmorillonite (a), and EXAFS spectra of Zn diluted into a dioctahedral (Redhill montmorillonite) and trioctahedral (ZnKer003, $Zn_{0.03}Mg_{2.97}Si_4O_{10}(OH)_2 \cdot nH_2O$) layer silicate (b).

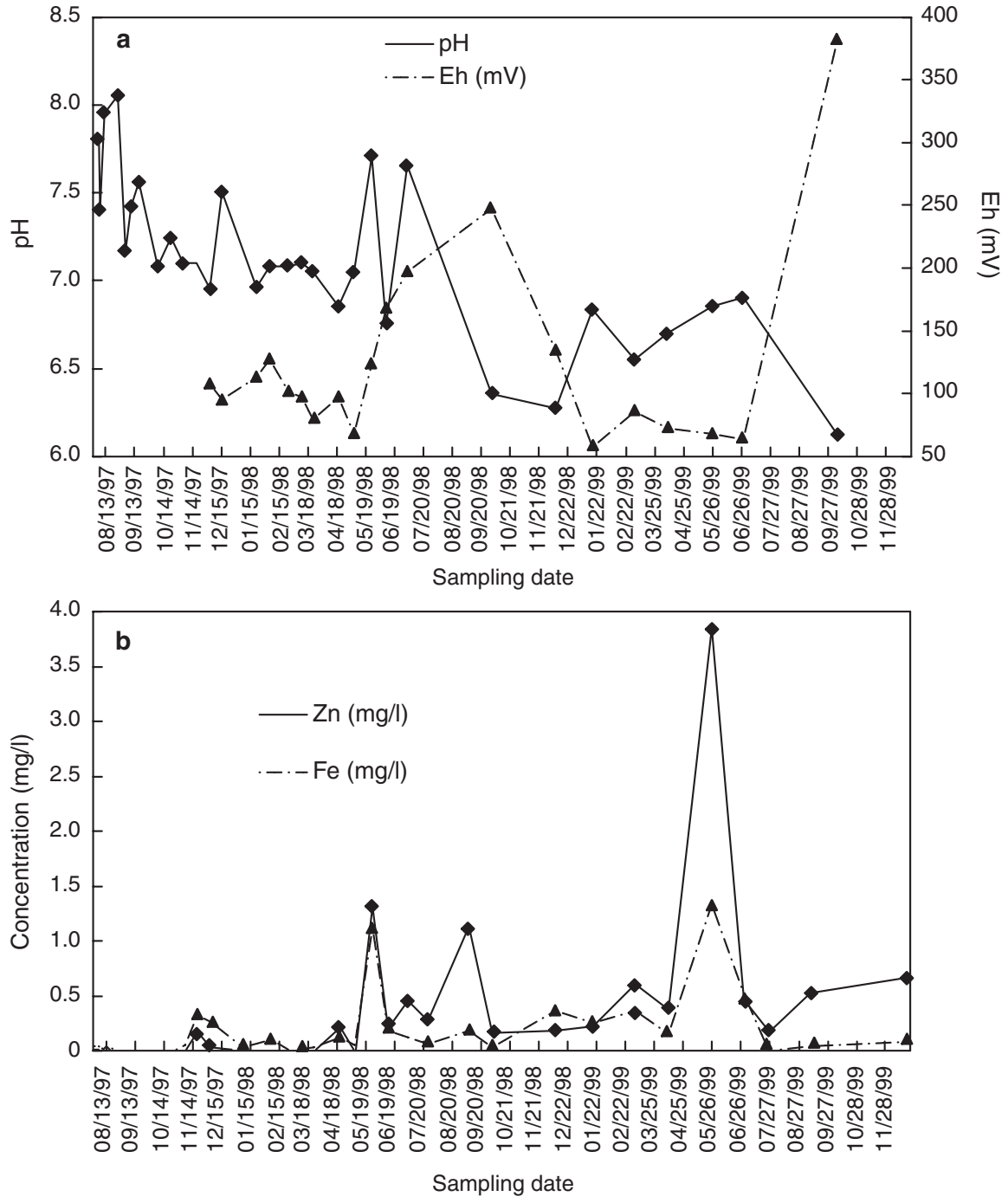
a
pH
Eh (mV)
pH
Eh (mV)
Sampling date
b
Zn (mg/l)
Fe (mg/l)
Concentration (mg/l)
Sampling date

**Fig. 1**

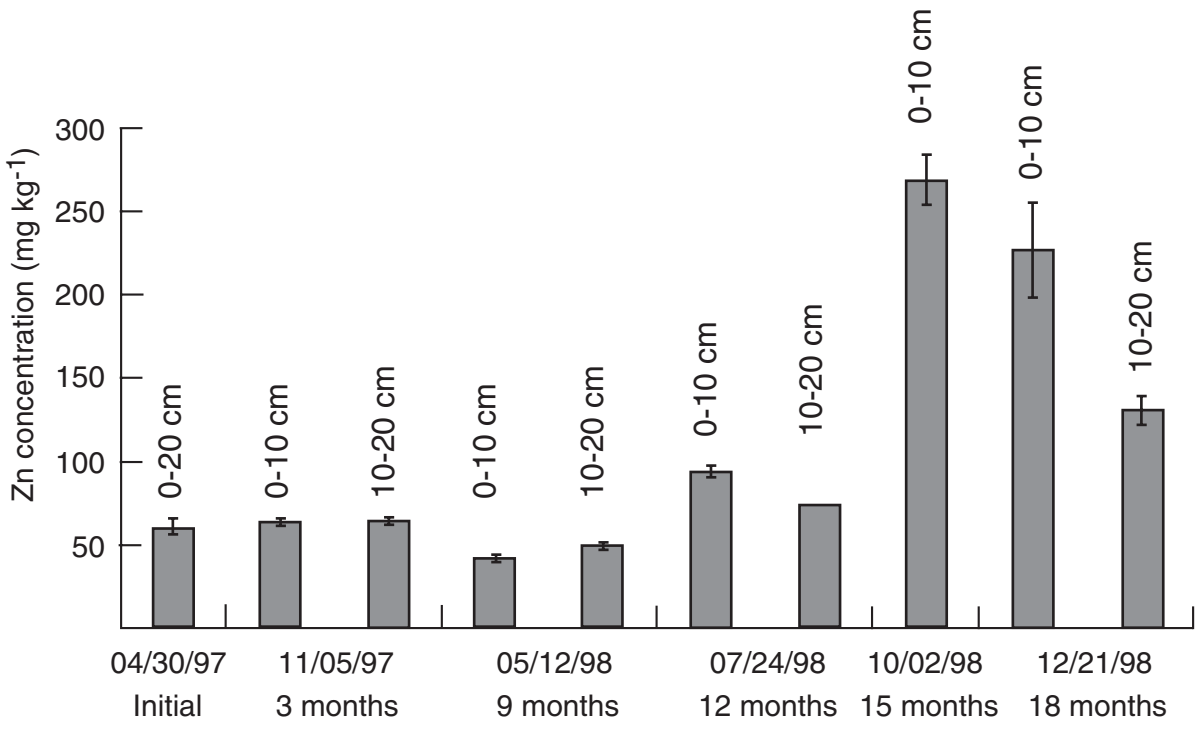
Zn concentration (mg kg-1)
300
250
200
150
100
50
0-20 cm
0-10 cm
10-20 cm
0-10 cm
10-20 cm
0-10 cm
10-20 cm
0-10 cm
0-10 cm
10-20 cm
04/30/97
Initial
11/05/97
3 months
05/12/98
9 months
07/24/98
12 months
10/02/98
15 months
12/21/98
18 months

**Fig. 2**

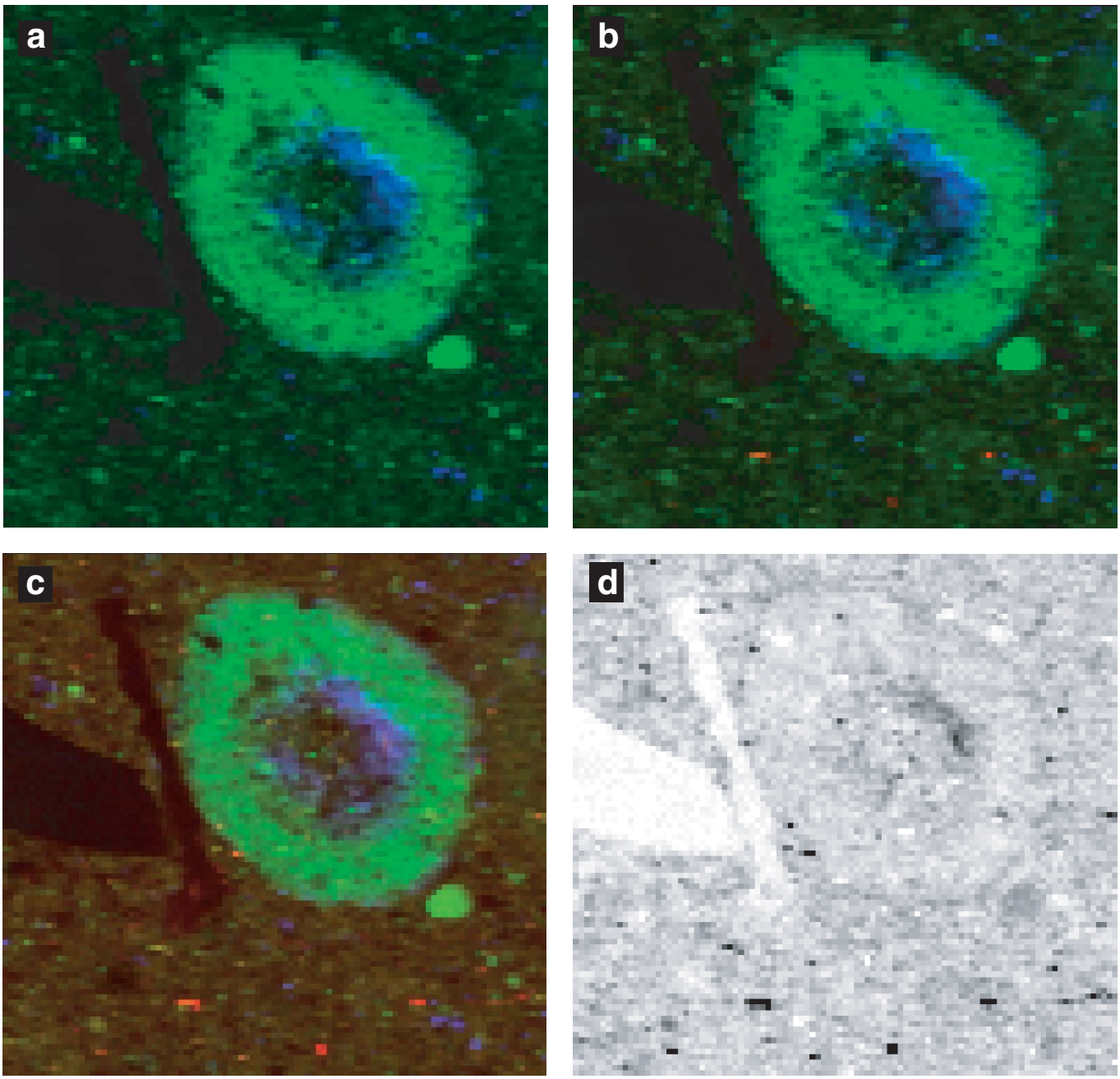


Fig. 03

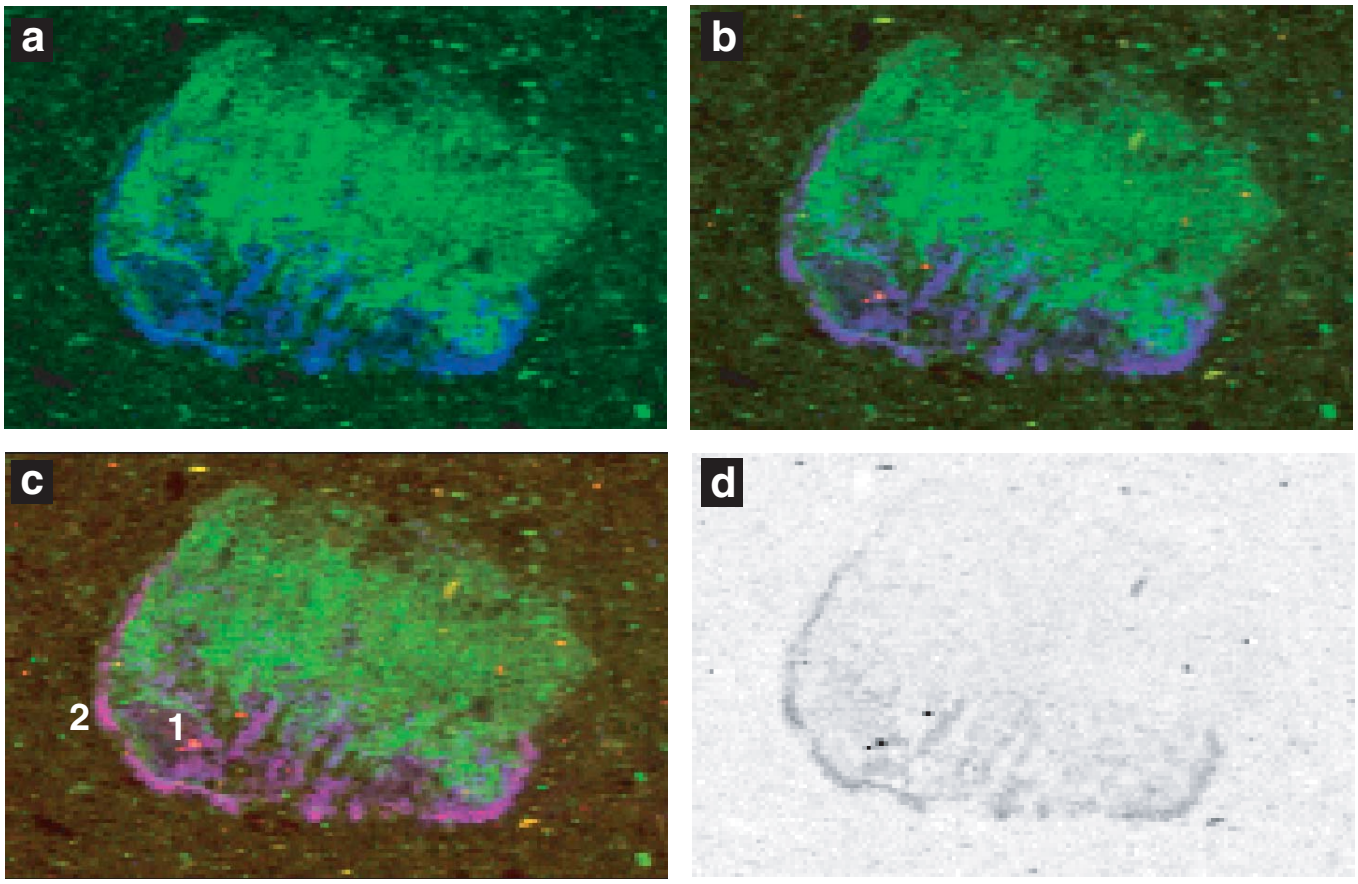


Fig. 04

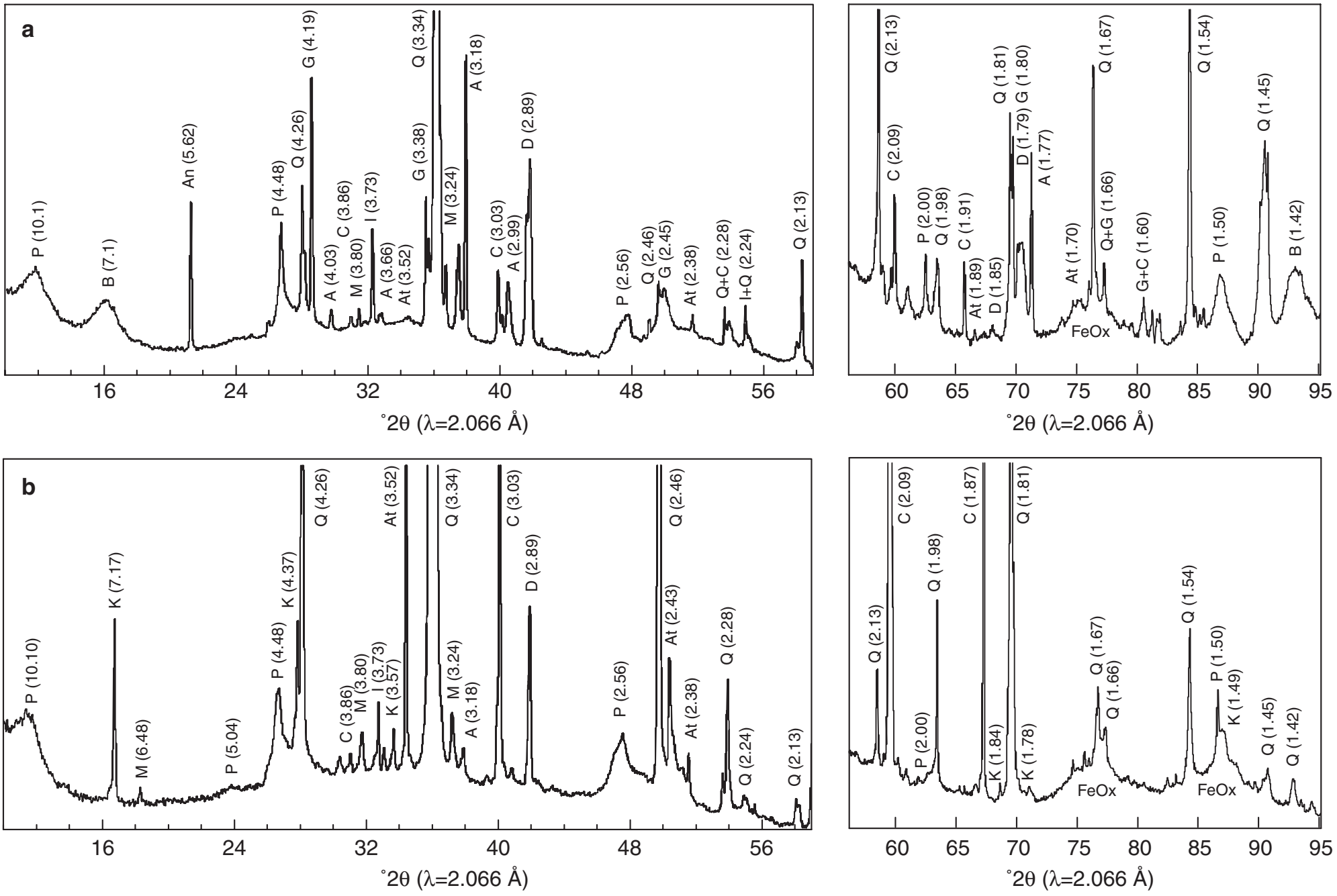
a
P (10.1)
B (7.1)
An (5.62)
P (4.48)
Q (4.26)
G (4.19)
A (4.03)
C (3.86)
M (3.80)
I (3.73)
A (3.66)
At (3.52)
G (3.38)
Q (3.34)
M (3.24)
A (3.18)
C (3.03)
A (2.99)
D (2.89)
P (2.56)
Q (2.46)
G (2.45)
At (2.38)
Q+C (2.28)
I+Q (2.24)
Q (2.13)
16
24
32
40
48
56
˚2θ (λ=2.066 Å)
Q (2.13)
C (2.09)
P (2.00)
Q (1.98)
C (1.91)
At (1.89)
D (1.85)
Q (1.81)
D (1.79)
G (1.80)
A (1.77)
At (1.70)
FeOx
Q (1.67)
Q+G (1.66)
G+C (1.60)
Q (1.54)
P (1.50)
Q (1.45)
B (1.42)
60
65
70
75
80
85
90
95
˚2θ (λ=2.066 Å)
b
P (10.10)
K (7.17)
M (6.48)
P (5.04)
P (4.48)
K (4.37)
Q (4.26)
C (3.86)
M (3.80)
I (3.73)
K (3.57)
At (3.52)
Q (3.34)
M (3.24)
A (3.18)
C (3.03)
D (2.89)
P (2.56)
At (2.43)
Q (2.46)
At (2.38)
Q (2.28)
Q (2.24)
Q (2.13)
16
24
32
40
48
56
˚2θ (λ=2.066 Å)
Q (2.13)
C (2.09)
P (2.00)
Q (1.98)
C (1.87)
K (1.84)
K (1.78)
Q (1.81)
FeOx
Q (1.67)
Q (1.66)
FeOx
Q (1.54)
P (1.50)
K (1.49)
Q (1.45)
Q (1.42)
60
65
70
75
80
85
90
95
˚2θ (λ=2.066 Å)

**Fig. 5**

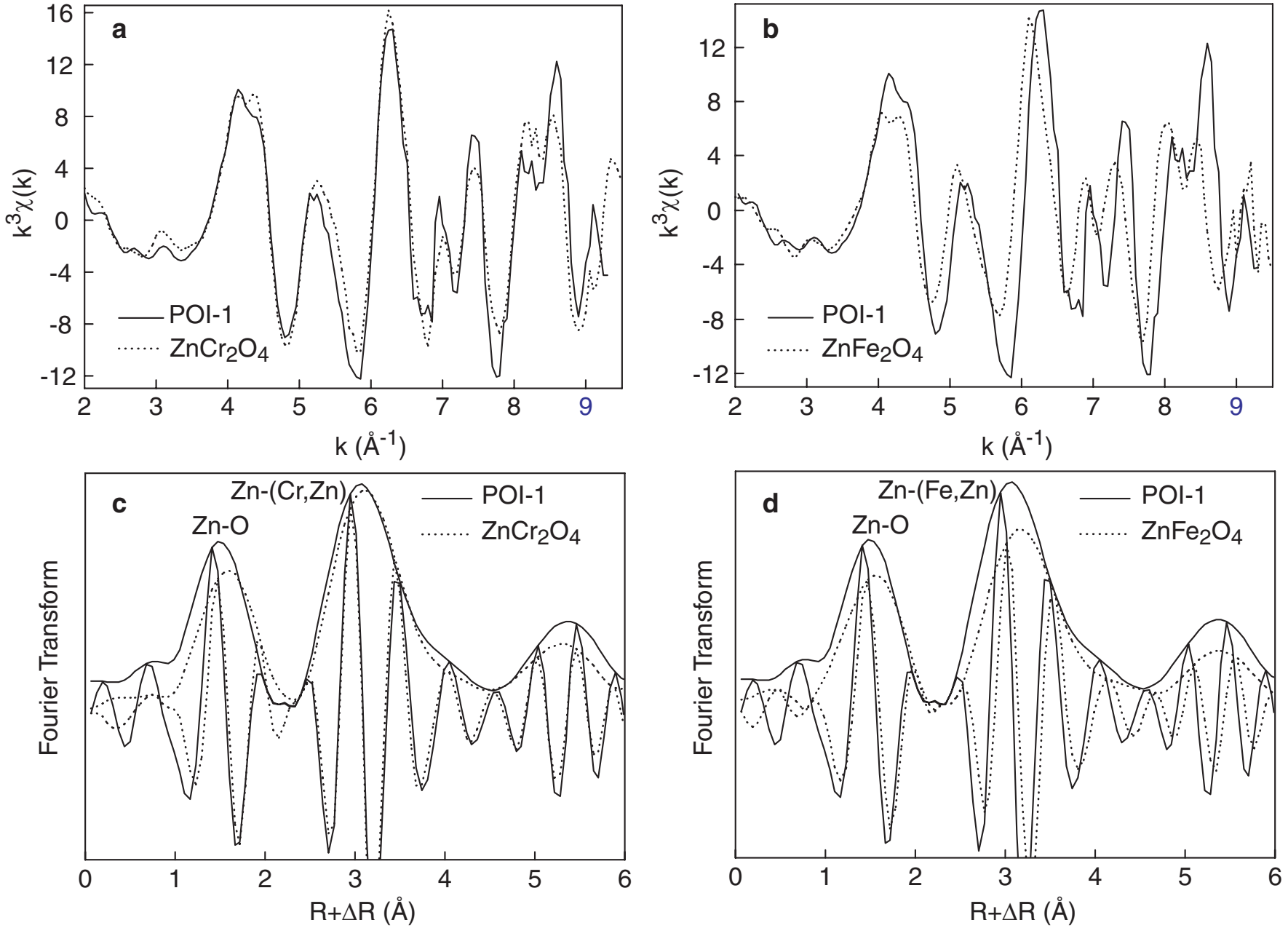
a
b
c
d
POI-1
$ZnCr_2O_4$
$ZnFe_2O_4$
$k^3\chi(k)$
k (Å$^{-1}$)
Fourier Transform
R+ΔR (Å)
Zn-O
Zn-(Cr,Zn)
Zn-(Fe,Zn)

**Fig. 6**

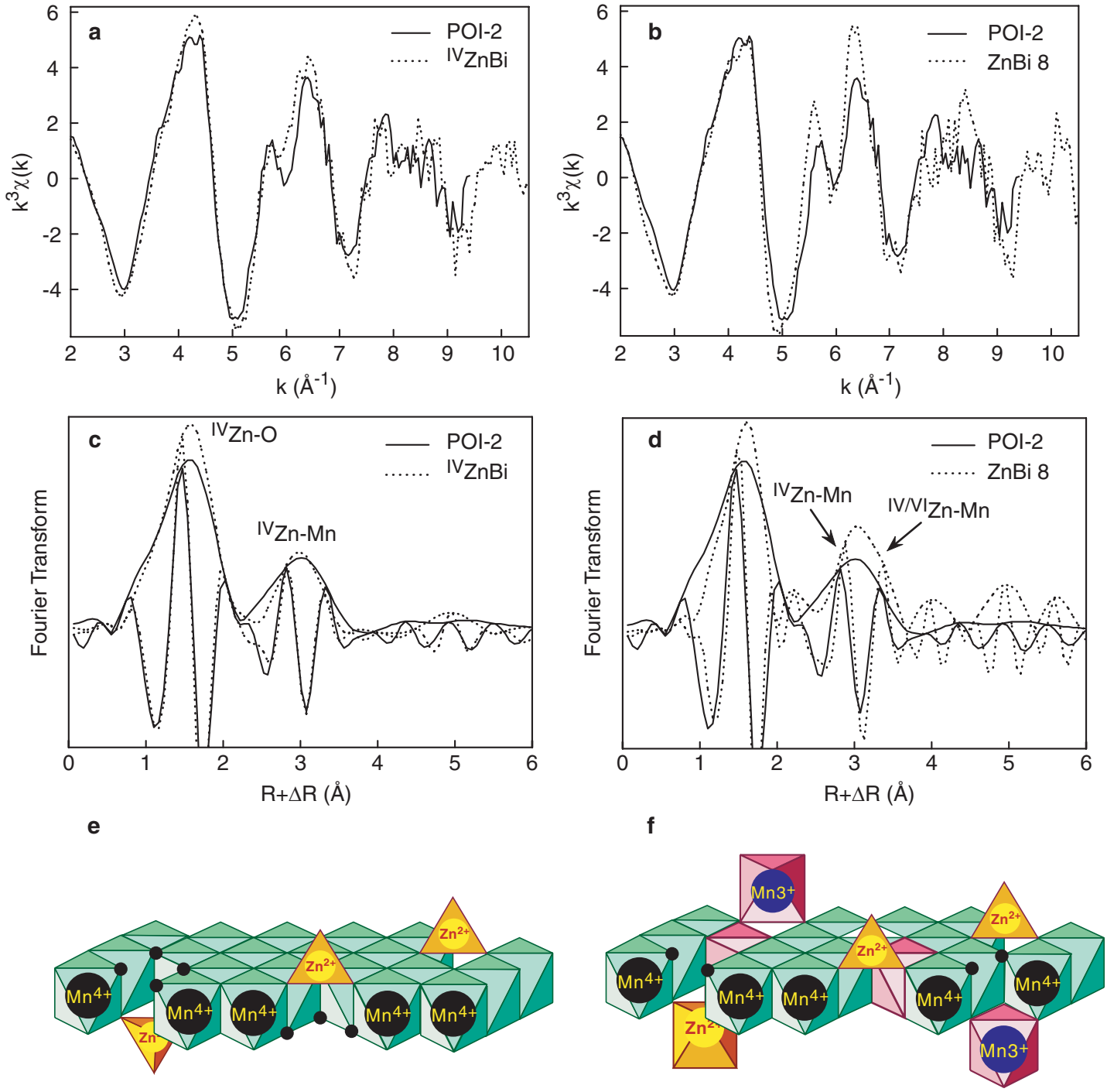
a
POI-2
IVZnBi
k3χ(k)
k (Å-1)
b
POI-2
ZnBi 8
k3χ(k)
k (Å-1)
c
IVZn-O
IVZn-Mn
POI-2
IVZnBi
Fourier Transform
R+ΔR (Å)
d
IVZn-Mn
IV/VIZn-Mn
POI-2
ZnBi 8
Fourier Transform
R+ΔR (Å)
e
Mn4+
Zn2+
Zn
f
Mn3+
Zn2+
Mn4+

Fig. 7

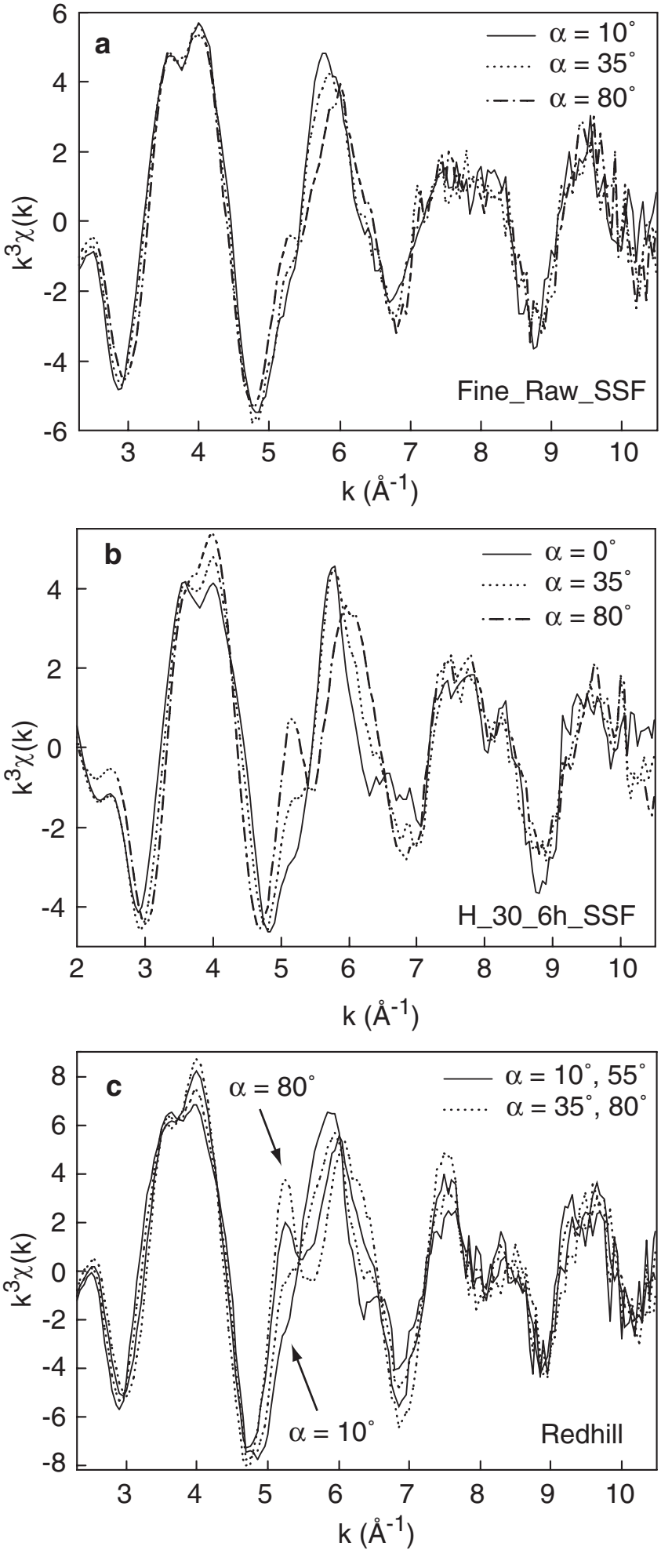
a
α = 10°
α = 35°
α = 80°
Fine_Raw_SSF
k³χ(k)
k (Å⁻¹)
b
α = 0°
α = 35°
α = 80°
H_30_6h_SSF
k³χ(k)
k (Å⁻¹)
c
α = 80°
α = 10°, 55°
α = 35°, 80°
α = 10°
Redhill
k³χ(k)
k (Å⁻¹)

**Fig. 8**

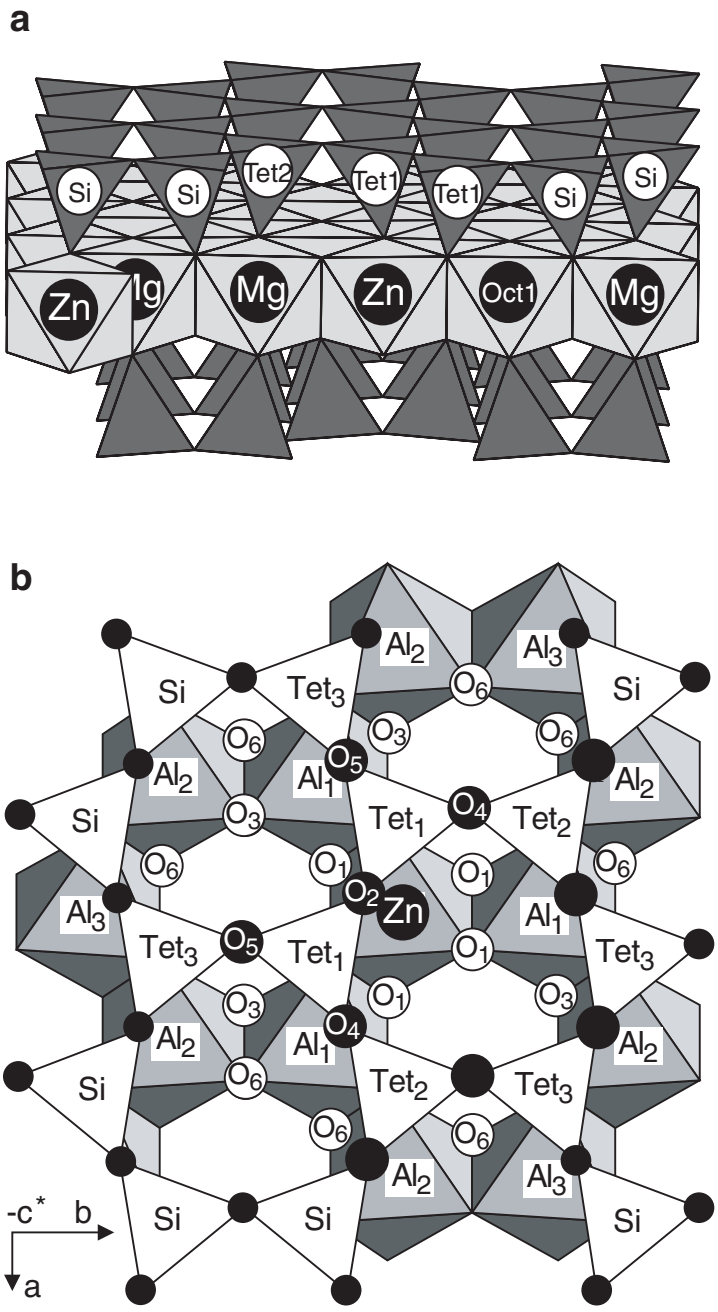
a
Si
Si
Tet2
Tet1
Tet1
Si
Si
Zn
Mg
Mg
Zn
Oct1
Mg
b
Si
Tet3
Al2
Al3
O6
Si
O6
O3
O6
O5
Al2
Al1
Al2
Si
O3
Tet1
O4
Tet2
O6
O1
O1
O6
O2
Zn
Al3
Al1
O5
Tet3
Tet1
O1
Tet3
O3
O1
O3
Al2
Al1
O4
Al2
Si
O6
Tet2
Tet3
O6
O6
Al2
Al3
-c*
b
a
Si
Si
Si

**Fig. 9**

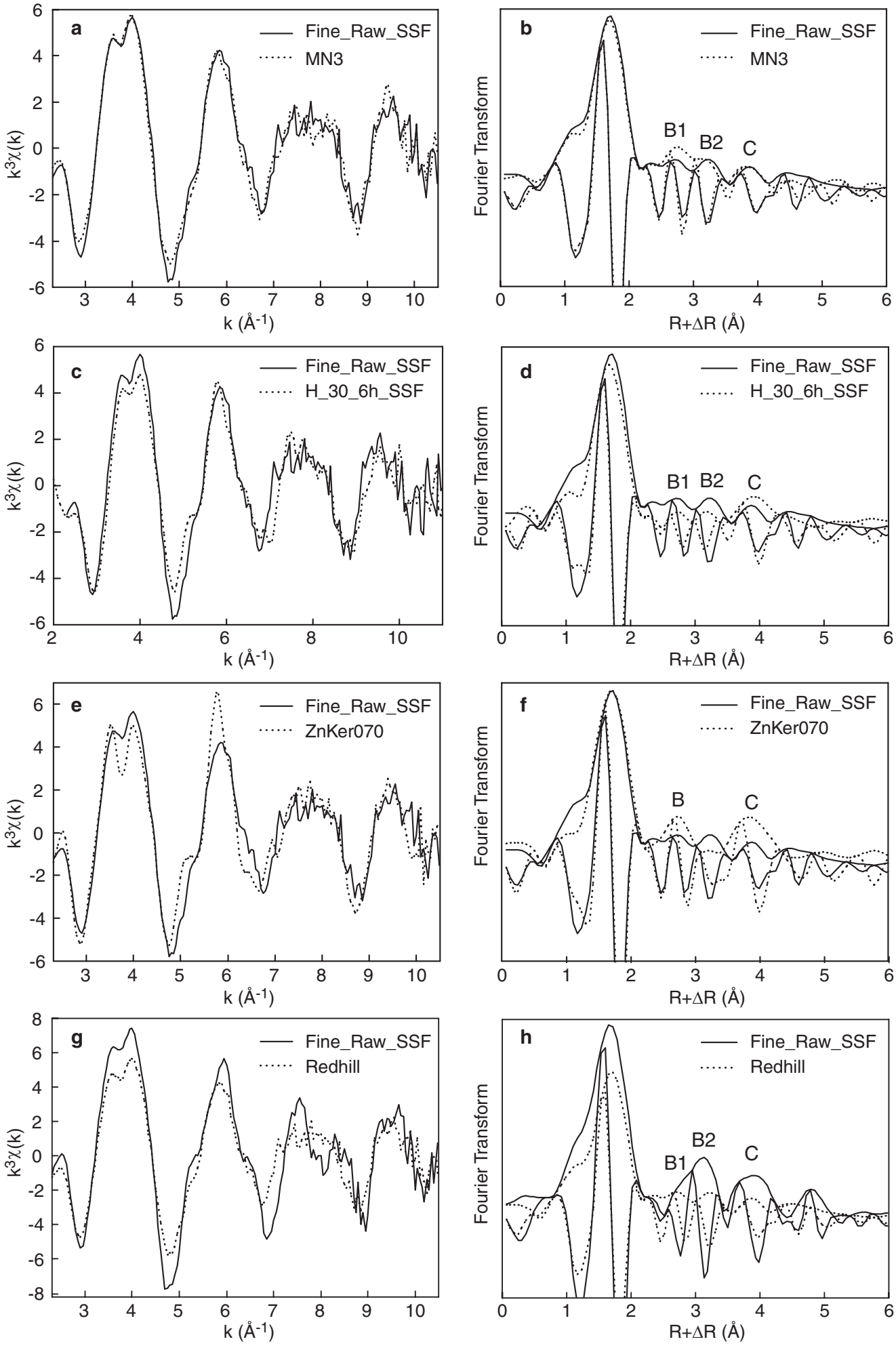
a
Fine_Raw_SSF
MN3
k³χ(k)
k (Å⁻¹)
b
Fine_Raw_SSF
MN3
B1
B2
C
Fourier Transform
R+ΔR (Å)
c
Fine_Raw_SSF
H_30_6h_SSF
k³χ(k)
k (Å⁻¹)
d
Fine_Raw_SSF
H_30_6h_SSF
B1 B2
C
Fourier Transform
R+ΔR (Å)
e
Fine_Raw_SSF
ZnKer070
k³χ(k)
k (Å⁻¹)
f
Fine_Raw_SSF
ZnKer070
B
C
Fourier Transform
R+ΔR (Å)
g
Fine_Raw_SSF
Redhill
k³χ(k)
k (Å⁻¹)
h
Fine_Raw_SSF
Redhill
B1
B2
C
Fourier Transform
R+ΔR (Å)

**Fig. 10-A**

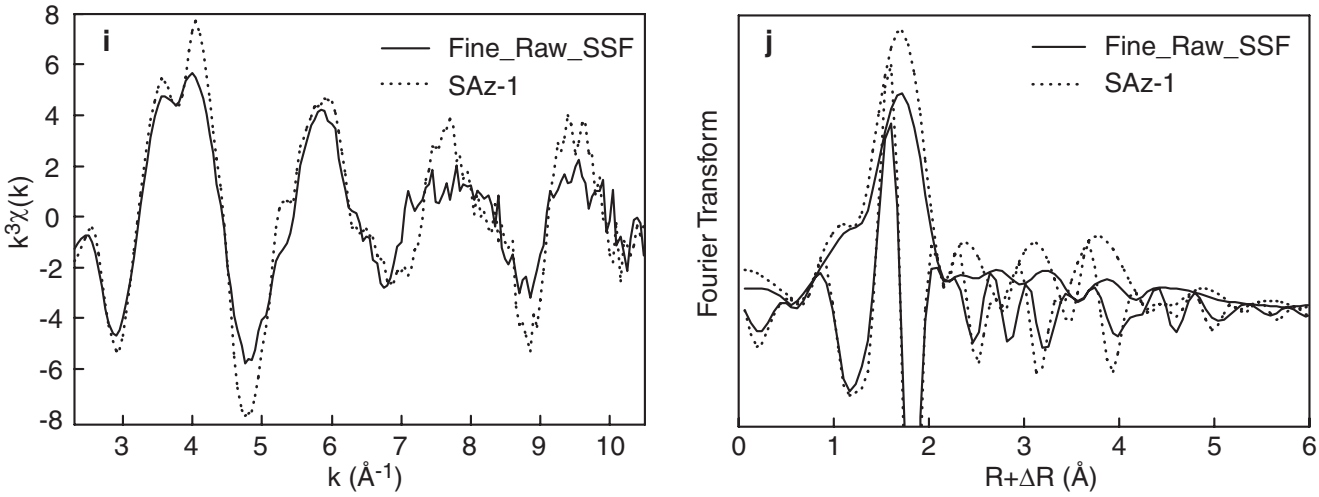
i
Fine_Raw_SSF
SAz-1
k³χ(k)
k (Å⁻¹)
8
6
4
2
0
-2
-4
-6
-8
3
4
5
6
7
8
9
10
j
Fine_Raw_SSF
SAz-1
Fourier Transform
R+ΔR (Å)
0
1
2
3
4
5
6

**Fig. 10-B**

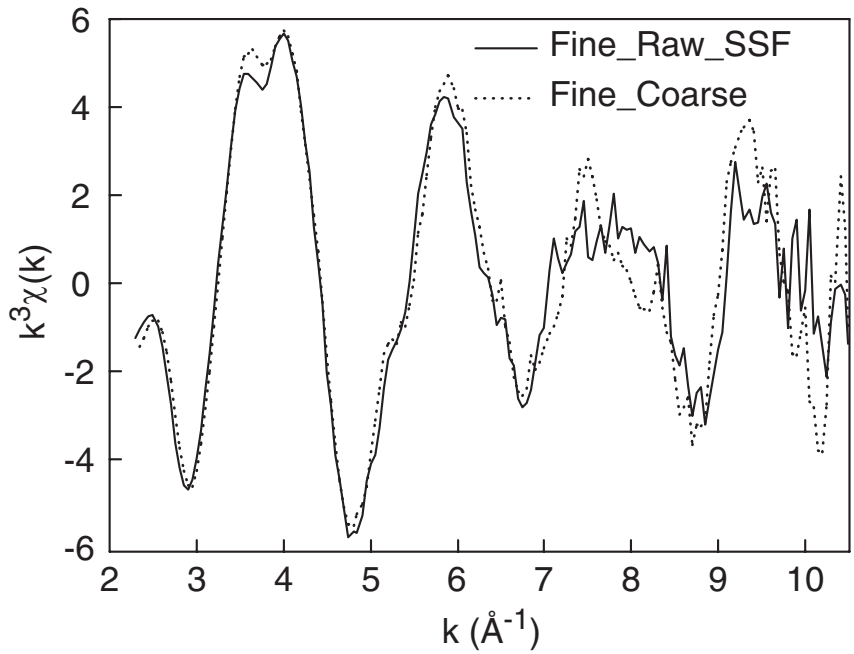


**Fig. 11**

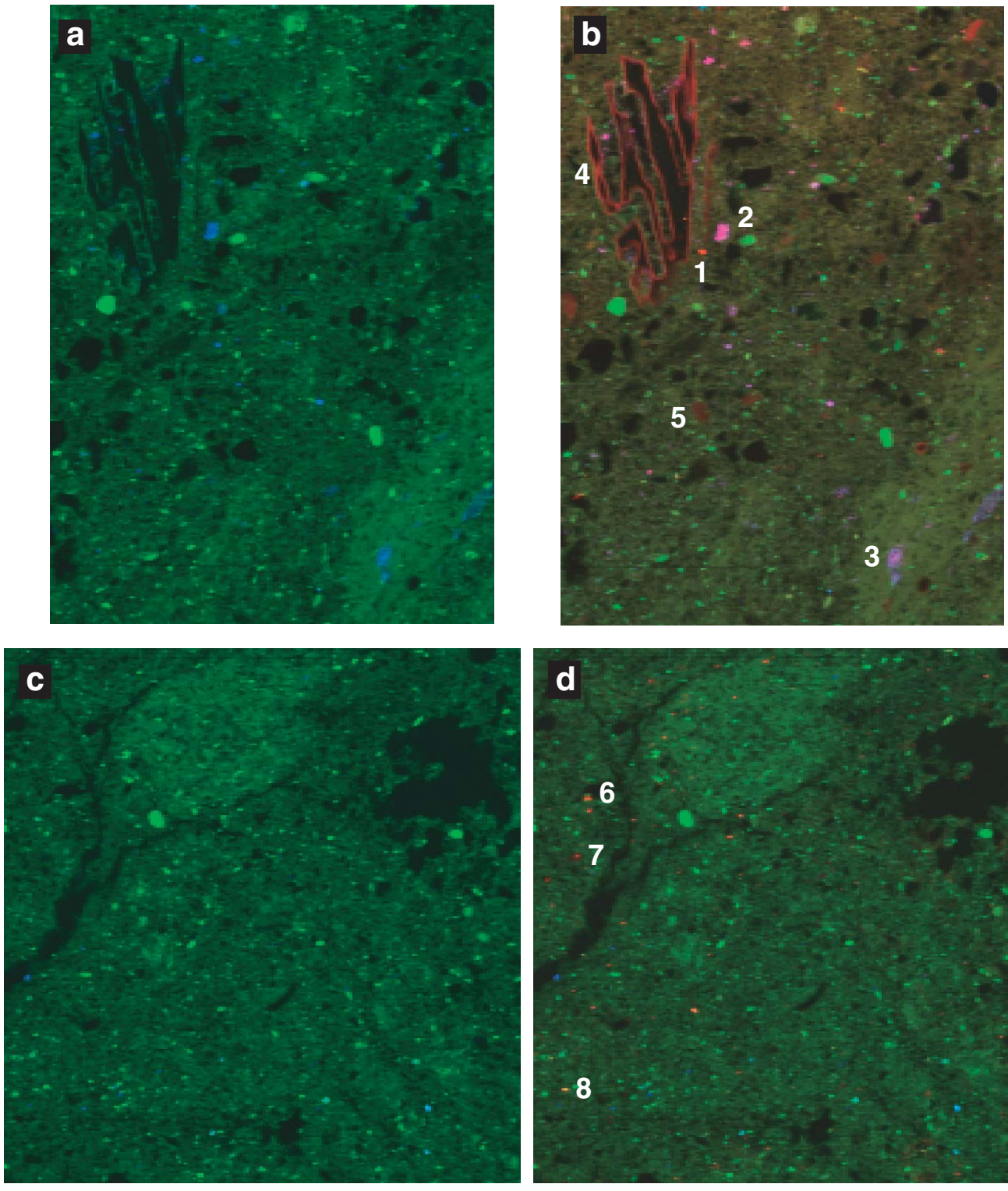


Fig. 12

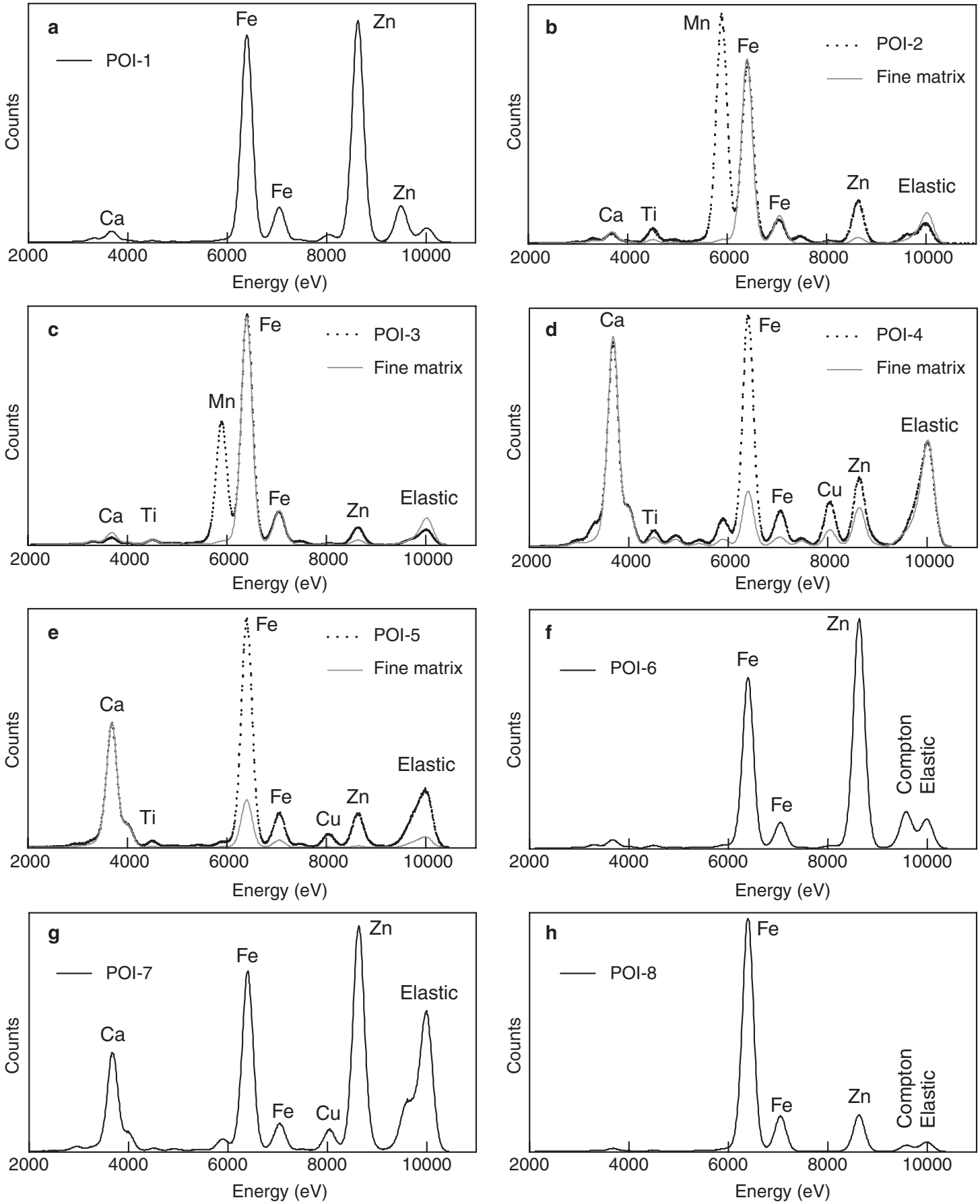
a
POI-1
Fe
Zn
Ca
Fe
Zn
Counts
2000
4000
6000
8000
10000
Energy (eV)
b
Mn
Fe
POI-2
Fine matrix
Ca
Ti
Fe
Zn
Elastic
c
Fe
POI-3
Fine matrix
Mn
Ca
Ti
Fe
Zn
Elastic
d
Ca
Fe
POI-4
Fine matrix
Elastic
Zn
Cu
Fe
Ti
e
Fe
POI-5
Fine matrix
Ca
Elastic
Ti
Fe
Zn
Cu
f
Zn
Fe
POI-6
Compton
Elastic
Fe
g
Zn
Fe
POI-7
Elastic
Ca
Fe
Cu
h
Fe
POI-8
Zn
Fe
Compton
Elastic

**Fig. 13**

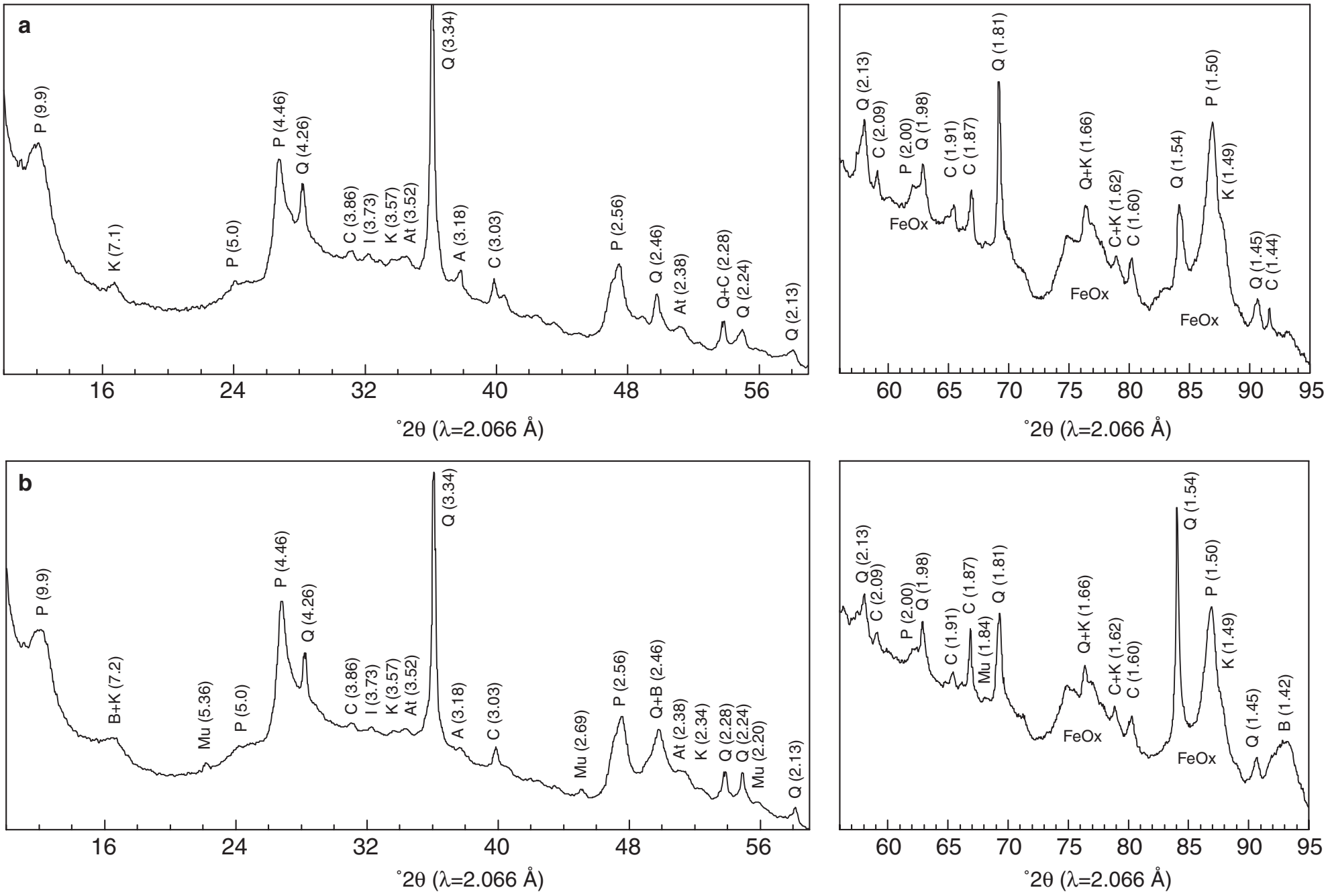
a
P (9.9)
K (7.1)
P (5.0)
P (4.46)
Q (4.26)
C (3.86)
I (3.73)
K (3.57)
At (3.52)
Q (3.34)
A (3.18)
C (3.03)
P (2.56)
Q (2.46)
At (2.38)
Q+C (2.28)
Q (2.24)
Q (2.13)
16
24
32
40
48
56
°2θ (λ=2.066 Å)
Q (2.13)
C (2.09)
P (2.00)
Q (1.98)
C (1.91)
C (1.87)
Q (1.81)
Q+K (1.66)
C+K (1.62)
C (1.60)
Q (1.54)
P (1.50)
K (1.49)
Q (1.45)
C (1.44)
FeOx
FeOx
FeOx
60
65
70
75
80
85
90
95
°2θ (λ=2.066 Å)
b
P (9.9)
B+K (7.2)
Mu (5.36)
P (5.0)
P (4.46)
Q (4.26)
C (3.86)
I (3.73)
K (3.57)
At (3.52)
Q (3.34)
A (3.18)
C (3.03)
Mu (2.69)
P (2.56)
Q+B (2.46)
At (2.38)
K (2.34)
Q (2.28)
Q (2.24)
Mu (2.20)
Q (2.13)
16
24
32
40
48
56
°2θ (λ=2.066 Å)
Q (2.13)
C (2.09)
P (2.00)
Q (1.98)
C (1.91)
C (1.87)
Mu (1.84)
Q (1.81)
Q+K (1.66)
C+K (1.62)
C (1.60)
Q (1.54)
P (1.50)
K (1.49)
Q (1.45)
B (1.42)
FeOx
FeOx
60
65
70
75
80
85
90
95
°2θ (λ=2.066 Å)

**Fig. 14**

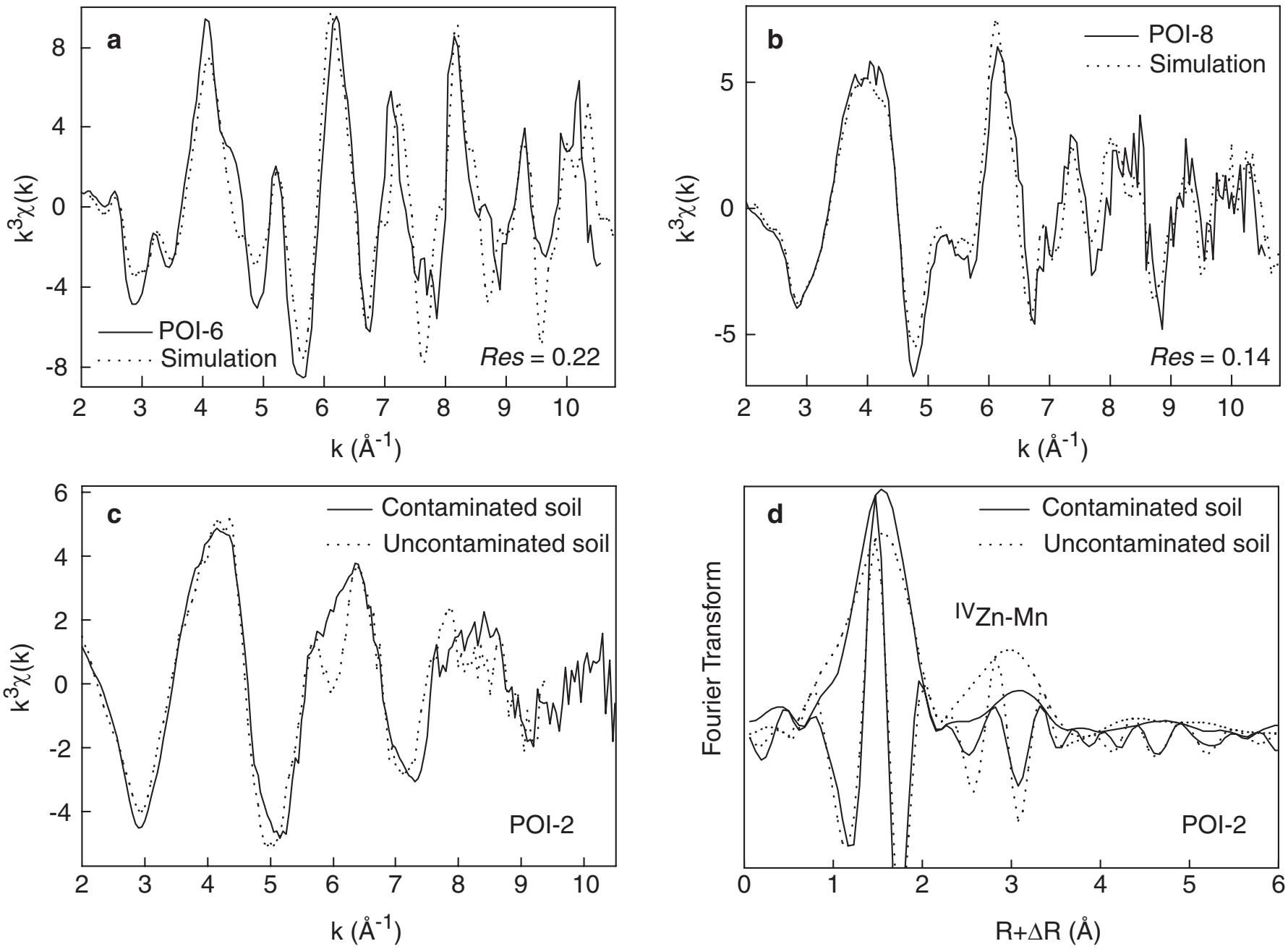
a
POI-6
Simulation
Res = 0.22
k³χ(k)
k (Å⁻¹)
b
POI-8
Simulation
Res = 0.14
k³χ(k)
k (Å⁻¹)
c
Contaminated soil
Uncontaminated soil
POI-2
k³χ(k)
k (Å⁻¹)
d
Contaminated soil
Uncontaminated soil
IVZn-Mn
POI-2
Fourier Transform
R+ΔR (Å)

**Fig. 15**

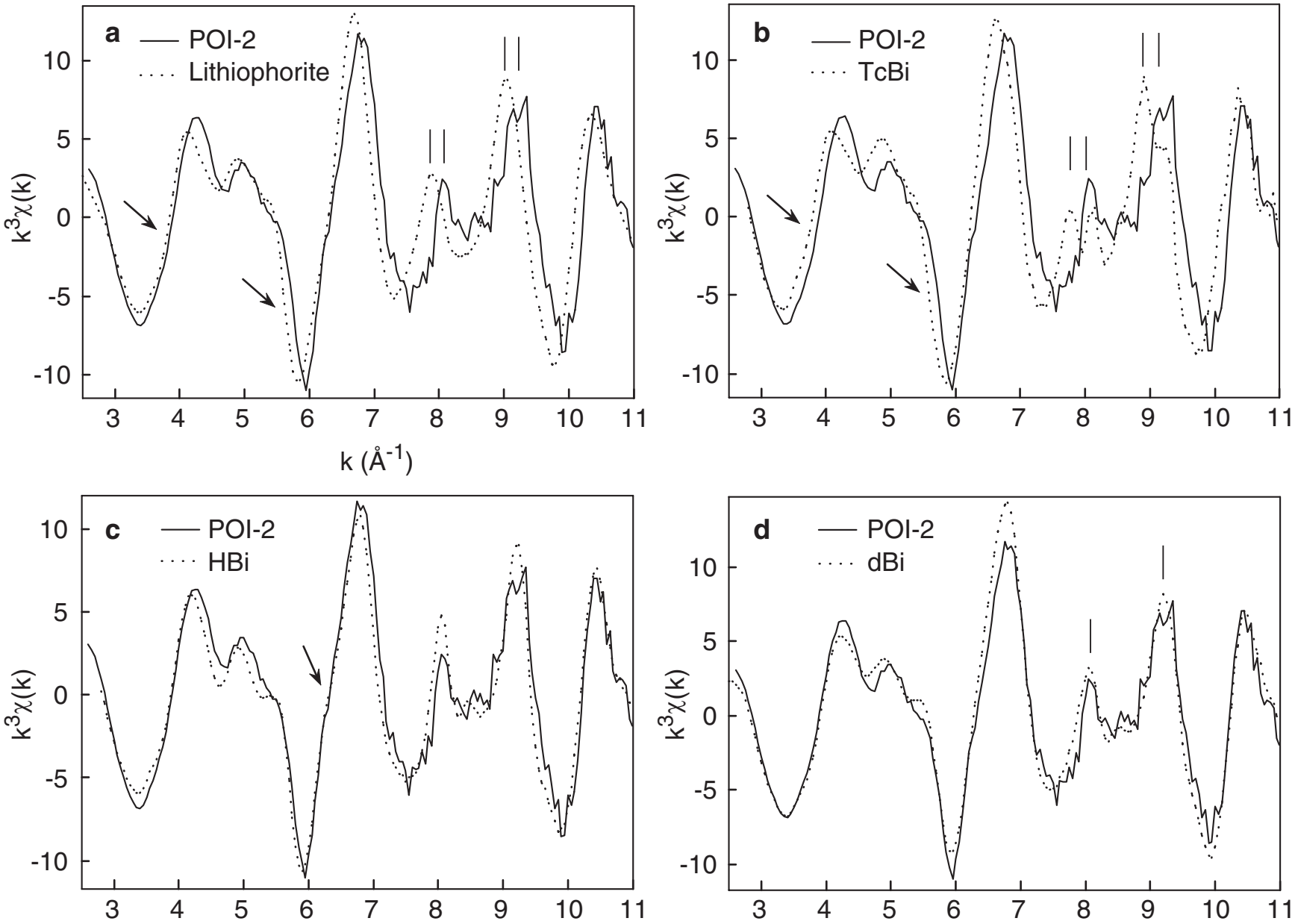
a
POI-2
Lithiophorite
b
POI-2
TcBi
c
POI-2
HBi
d
POI-2
dBi
k³χ(k)
k (Å⁻¹)

**Fig. 16**

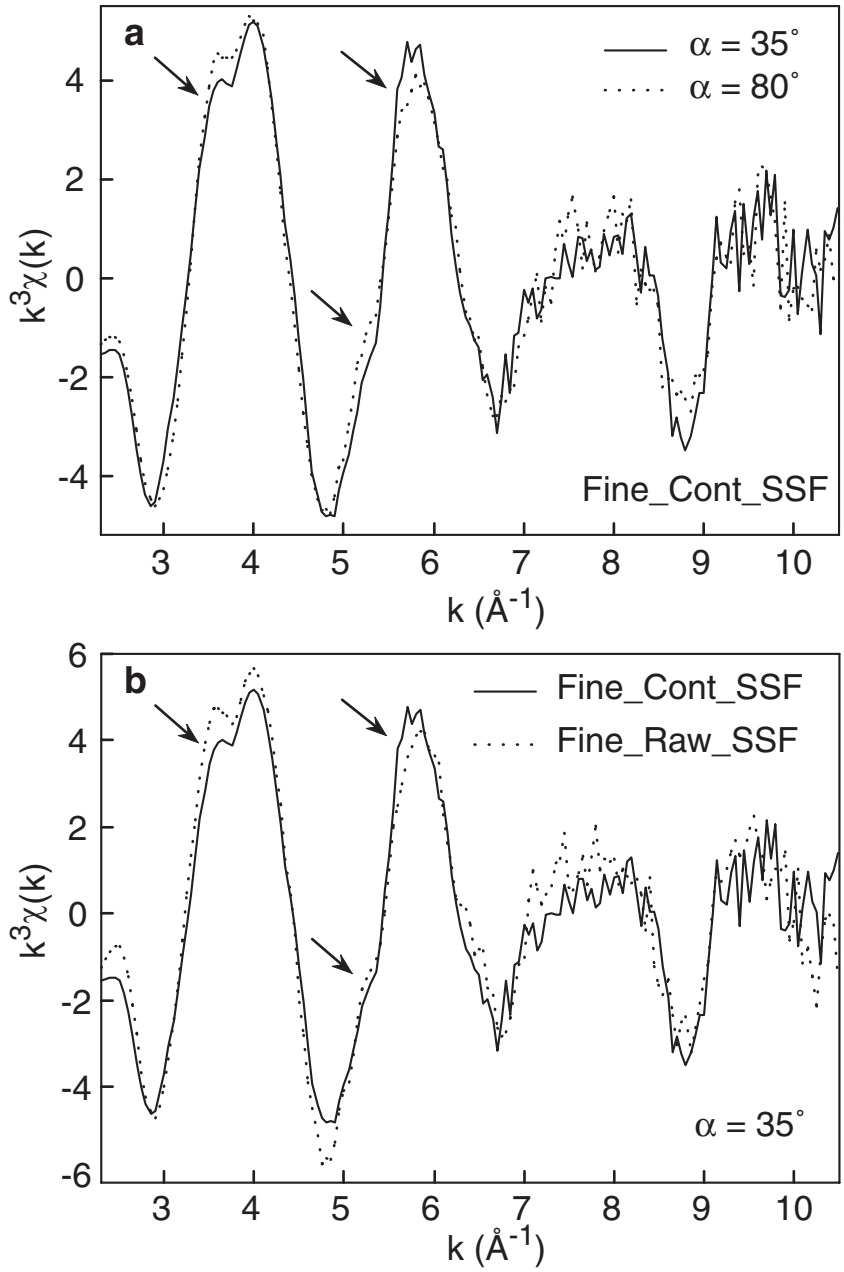
a
α = 35°
α = 80°
Fine_Cont_SSF
k³χ(k)
k (Å⁻¹)
b
Fine_Cont_SSF
Fine_Raw_SSF
α = 35°
k³χ(k)
k (Å⁻¹)

**Fig. 17**

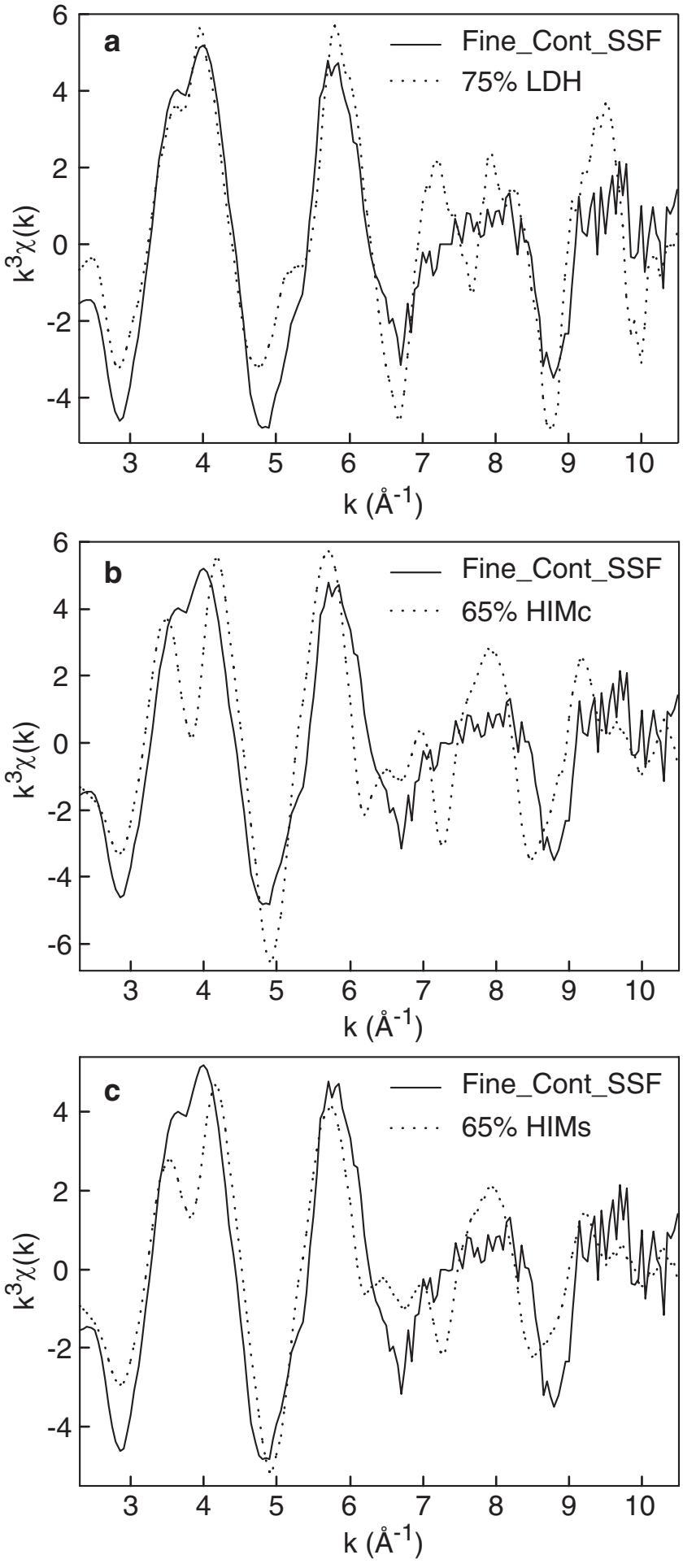
a
Fine_Cont_SSF
75% LDH
b
Fine_Cont_SSF
65% HIMc
c
Fine_Cont_SSF
65% HIMs
k³χ(k)
k (Å⁻¹)

**Fig. 18**

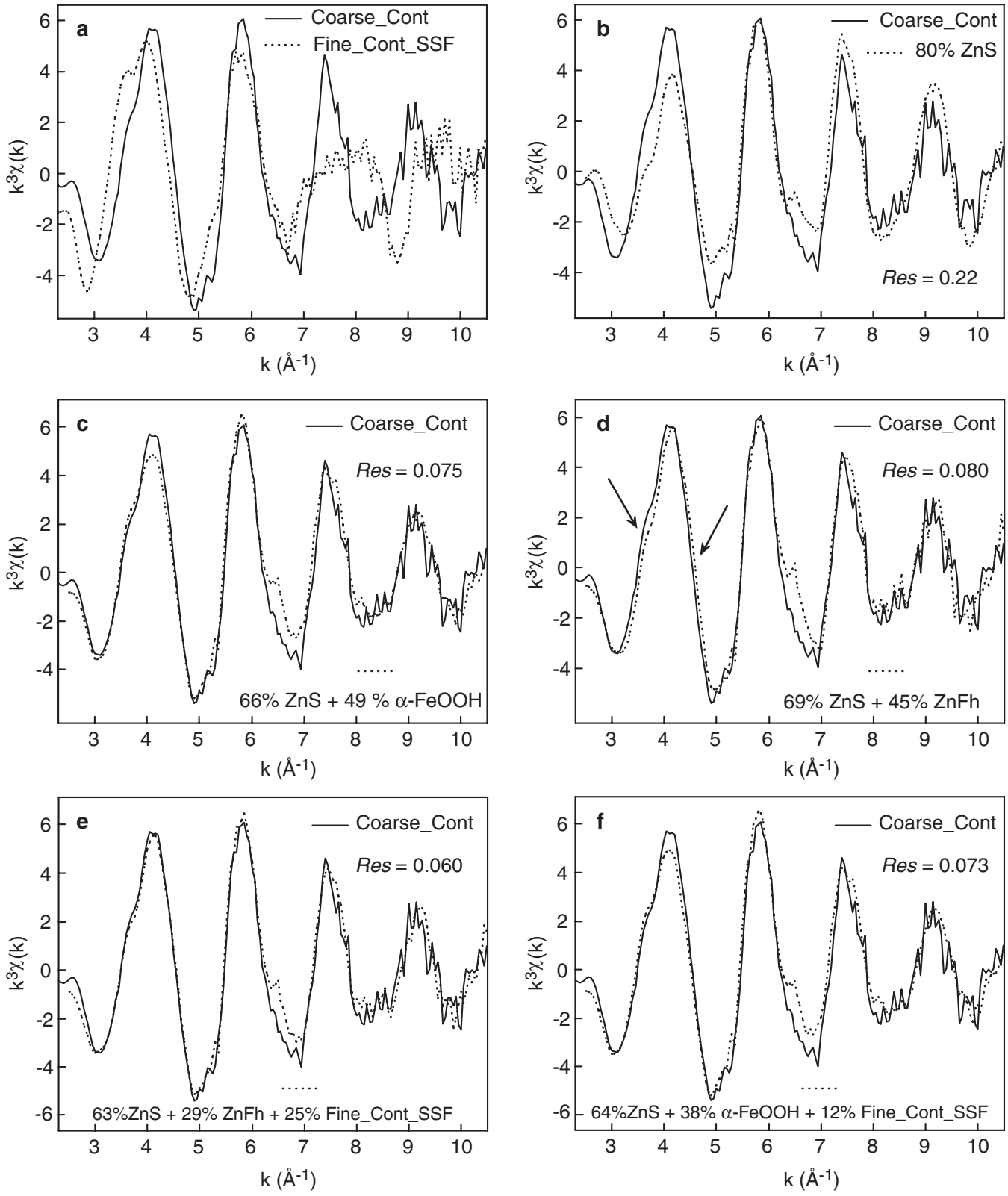
a
Coarse_Cont
Fine_Cont_SSF
b
Coarse_Cont
80% ZnS
Res = 0.22
c
Coarse_Cont
Res = 0.075
66% ZnS + 49 % α-FeOOH
d
Coarse_Cont
Res = 0.080
69% ZnS + 45% ZnFh
e
Coarse_Cont
Res = 0.060
63%ZnS + 29% ZnFh + 25% Fine_Cont_SSF
f
Coarse_Cont
Res = 0.073
64%ZnS + 38% α-FeOOH + 12% Fine_Cont_SSF
k³χ(k)
k (Å⁻¹)

**Fig. 19**

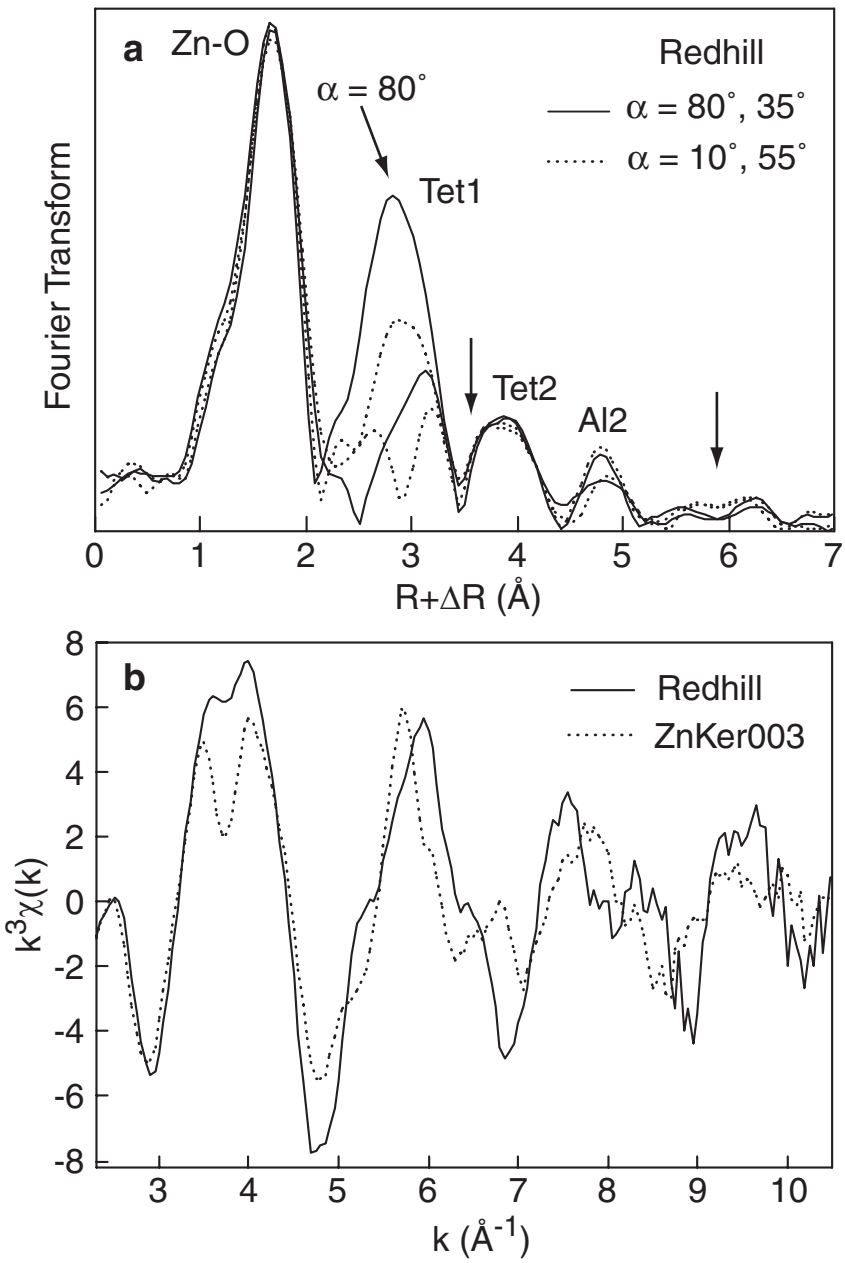
a
Zn-O
α = 80°
Tet1
Tet2
Al2
Redhill
α = 80°, 35°
α = 10°, 55°
Fourier Transform
R+ΔR (Å)
b
Redhill
ZnKer003
k³χ(k)
k (Å⁻¹)

**Fig. 20**